Impact of thermal maturity on the concomitant evolution of the ultrafine structure and porosity of marine mudstones organic matter; contributions of electronic imaging and new spectroscopic investigations

Amélie Cavelan, Mohammed Boussafir, Nathalie Mathieu, Fatima Laggoun-Défarge

HAL Id: insu-02977988

https://insu.hal.science/insu-02977988

Submitted on 26 Oct 2020

Journal Pre-proof

Impact of thermal maturity on the concomitant evolution of the ultrafine structure and porosity of marine mudstones organic matter; contributions of electronic imaging and new spectroscopic investigations

Amélie Cavelan, Mohammed Boussafir, Nathalie Mathieu, Fatima Laggoun-Défarge

Please cite this article as: A. Cavelan, M. Boussafir, N. Mathieu, et al., Impact of thermal maturity on the concomitant evolution of the ultrafine structure and porosity of marine mudstones organic matter; contributions of electronic imaging and new spectroscopic investigations, *International Journal of Coal Geology* (2020), https://doi.org/10.1016/j.coal.2020.103622

Impact of thermal maturity on the concomitant evolution of the ultrafine structure and porosity of marine mudstones organic matter; contributions of electronic imaging and new spectroscopic investigations.

Amélie Cavelan[a,b,*] amelie.cavelan@etu.univ-orleans.fr, Mohammed Boussafir[a,c], Nathalie Mathieu[d], Fatima Laggoun-Défarge[a]

[a]Université d'Orléans, CNRS, BRGM, ISTO, UMR 7327, F-45071, Orléans, France

[b]Université de Lorraine, CNRS, LIEC, UMR 7360, F-54500, Vandoeuvre les Nancy, France

[c]Université François Rabelais de Tours, EA 6293 GéHCO, Tours, France

[d]Université d'Orléans, CNRS, ICMN, UMR 7374, 45071 Orléans, France

[*]Corresponding author.

Abstract

This study aims to better understand the evolution of the organic matter (OM) ultrafine structure (designating the nanoscopic structure of the OM/macerals) and porosity with increasing thermal maturity of mudstones source-rocks. To this end, the particulate fractions of kerogen from organic-rich Kimmeridge clay mudstones were isolated by acidic treatment before and after laboratory thermal

maturation. The evolution of the composition, the chemical structure and the porosity of kerogen from the immature stage (Ro=0.42%) to the dry gas zone (Ro=2.12%) were documented using a combination of elemental analysis, vitrinite reflectance measurements, Scanning Electron Microscopy (SEM) and Transmission Electron Microscopy (TEM), Raman spectroscopy and Small Angle X-Ray Scattering (SAXS). The evolution of the porosity of OM was then compared to the evolution of the pore volume of the total rock measured by nitrogen adsorption. The results show that the progressive densification, reorganization and aromatization of the amorphous kerogen particles into a more ordered, but heterogeneous carbon-rich residue is responsible for significant variations in the kerogen porosity with increasing maturity. Contrary to the previous observations on these Kimmeridge clay mudstones, the variations that occur during the peak of oil generation (Ro of ca. 0.90%) mark the onset of the OM-hosted pores development. There appears to be a natural close relationship between the evolution of OM porosity and total pore volume of organic-rich mudstones during gas generation. Indeed, a similar alternation of pore collapse and pore development is observed in response to gas generation. The development and the evolution of pores in these organic-rich mudstones seems thus mainly driven by the evolution of the chemical structure and the composition of OM during thermal maturation. In the dry gas zone, the porosity and the specific surface area of the kerogen are significant (19% and 57.1 $m^2.g^{-2}$ respectively). This highlights the importance of the OM content, type and composition in the porosity and gas storage capacities of mudstone reservoirs, increasingly discussed in the available literature in recent years.

Keywords: mudstone; ultrafine OM structure; TEM; SAXS; Raman spectroscopy.

1. Introduction

The porosity of organic-rich mudstones is generally dominated by mesopores (2–50 nm pore size as defined in Rouquerol et al., 1994) but it can also contain variable amounts of macropores (> 50 nm) and micropores (< 2 nm) (Chalmers et al., 2012a; Chalmers and Bustin, 2008; Mastalerz et al., 2013; Ross and Bustin, 2009). Due to this wide range of pore sizes, a combination of different techniques is often required for the assessment of porosity. High magnification imaging techniques such as scanning electron microscopy (SEM) and transmission electron microscopy (TEM) coupled with an argon-ion-beam milling for sample preparation have provided many information on the distribution, the size of pores and the evolution of the porosity of mudstones with burial (Bernard et al., 2012; Curtis et al., 2012; Fishman et al., 2012; Hackley et al., 2017; Keel, 2015; Ko et al., 2018; Loucks et al., 2012; Rodriguez et al., 2014; Romero-Sarmiento et al., 2014). These high magnification techniques are not always sufficient to assess the full range of pore sizes that exists in these rocks. Previous studies reveal that a significant number of pores are often less than 5 nm (King et al., 2015; Klaver et al., 2015; Mathia et al., 2016). Regular imaging techniques are generally not able to fully assess the microporosity (<2 nm) and the mesoporosity (2-50 nm in diameter). For example, Mathia et al. (2016) found that the porosity estimated using SEM on the Lower Toarcian Posidonia Shale does not exceed 25% of the total rock porosity. Hence, other analytical approaches are commonly used such as gas adsorption measurements (Chalmers et al., 2012b; Chen and Xiao, 2014; Kuila et al., 2012; Pan et al., 2015; Rouquerol et al., 1994; Song et al., 2019; Tian et al., 2015, 2013) or Mercury intrusion porosimetry (Clarkson et al., 2013; Mastalerz et al., 2013). Each of these techniques provides information on different pore attributes or on various pore size ranges and cannot therefore be compared easily (Bustin et al., 2009; Clarkson et al., 2013; Mastalerz et al., 2012). Furthermore, the total porosity, not always well-interconnected, can be strongly different from the volume accessible to

gas or fluids flowing through the rock, hence the importance of combining these techniques with methods allowing the assessment of the total porosity such as small-angle and ultra-small angle neutron scattering (USANS and SANS) (Clarkson et al., 2013; Mastalerz et al., 2012) and small-angle X-ray scattering (SAXS) (Leu et al., 2016). This already complex situation is further complicated by the presence of a multitude of pore types associated both with the organic matter (OM) and the mineral matrix.

Previous investigations suggested that the OM is frequently one of the main components of organic-rich mudstone pore volume with increasing maturity (Chalmers et al., 2012a; Furmann et al., 2016; Han et al., 2019; Katz and Arango, 2018; Liu et al., 2018; Loucks et al., 2012; Mastalerz et al., 2013; Milliken et al., 2013; Pan et al., 2015; Song et al., 2019). A positive relationship is regularly observed between total organic carbon content (TOC), porosity and/or the volume of gas adsorbed in mudstones (Chalmers and Bustin, 2008; Han et al., 2019; Ma et al., 2015; Ross and Bustin, 2009; Song et al., 2019; Strąpoć et al., 2010; Tian et al., 2015, 2013; Wang et al., 2013). Furthermore, the OM composition appears to strongly influence the evolution of porosity with burial (Cavelan et al., 2019a; Chen et al., 2015; Ko et al., 2018, 2017). This indicates that the formation and the evolution of mudstone reservoirs pore network may be largely driven by the OM type, content and composition.

The complex physico-chemical processes that occur during the thermal cracking of kerogen with burial lead to the progressive depletion in heteroatom-rich organic compounds by the release of hydrogenated and oxygenated and other heteroatom-rich chemical groups in the form of liquid and gaseous hydrocarbons and CO_2, H_2S or N_2 (Behar and Vandenbroucke, 1987; Peters et al., 2007; Tissot and Welte, 1984). During these phenomena, previous TEM studies have demonstrated that kerogen becomes enriched in nm-size graphene-like polyaromatic layers which tend to pile up into

increasingly well-ordered and larger basic structural units (Boulmier et al., 1982; Oberlin, 1989; Rouzaud and Oberlin, 1989). These works show that the reorientation of these randomly distributed basic structural units in parallel structures in kerogen may result in the formation of a nano-scale porosity. These physico-chemical transformations of kerogen with increasing thermal maturity may be largely involved in the development of the porosity of organic-rich mudstones and may probably explain why OM content, porosity and thermal maturation processes appear so closely linked in overmature mudstone reservoirs (Ardakani et al., 2018; Chalmers et al., 2012a; Chalmers and Bustin, 2008; Han et al., 2019; Katz and Arango, 2018; Ko et al., 2018; Kuila et al., 2014; Loucks et al., 2009; Milliken et al., 2013; Ross and Bustin, 2009; Song et al., 2019). For example, Romero-Sarmiento et al. (2014) proposed that the disorientation of the polyaromatic layers of kerogen at the nano-scale and the ensuing generation of nanopores is responsible for most of the pore development in overmature organic-rich mudstones such as the Barnett Mudstones. Alternatively, investigations by Keel (2015) suggest that the formation of pores in Type II and III kerogen is mainly due to the creation of void spaces formed by the release of volatiles which surround 'aromatic islands'. This led him to make the hypothesis that the formation of these aromatic units is tied to the restructuring of kerogen macromolecules and the increase in aromaticity during thermal maturation. These processes may be largely involved in the development of organic-rich mudstone porosity previously observed in many formations (Ardakani et al., 2018; Cavelan et al., 2019a; Chalmers et al., 2012a; Katz and Arango, 2018; Ko et al., 2018; Kuila et al., 2014; Loucks et al., 2012, 2009; Milliken et al., 2013; Song et al., 2019).

This work aims to better investigate the effect of the evolution of the OM chemical structure on the porosity of mudstones during burial. To this end, a Type II kerogen of organic-rich mudstones

from the Kimmeridge Clay Formation (KCF) was isolated by acidic treatment after anhydrous thermal

maturation. The concomitant evolution of the porosity, the chemical structure and composition of the

OM with increasing thermal maturity was assessed from the micro to the nano scale by the

combination of elemental analyses, SEM, TEM imaging techniques, Raman spectroscopy and small

angle X-ray scattering (SAXS). Vitrinite reflectance measurements served for the assessment of

thermal maturity before and after thermal maturation. The results were then compared to the evolution

of the total rock pore volume assessed by nitrogen adsorption.

2. Experiments

2.1 Samples

One sample was collected from the Kimmeridge Clay formation (KCF). This formation is considered

as the major source unit responsible for most of the North Sea conventional petroleum resources and

exhibit also a significant potential as an unconventional reservoir of hydrocarbons (Cornford, 1984;

Gallois, 2004). The studied organic-rich mudstone was sampled from the Ebberston borehole at 69.96

meters deep (Cleveland basin Yorkshire, UK, Cavelan et al., 2019b). In this area the formation

consists of 100 to 400 meters of organic-rich mudstones alternating with limestones, coccolith and

marls (Herbin et al., 1995; Rawson and Riley, 1982). The studied sample is immature (Req= 0.50%,

Rock Eval 6$^®$ Tmax = 428°C, Cavelan et al., 2019a), contains Type II marine kerogen and belongs to a

series that has been well documented these last decades (Boussafir et al., 1995a, 1995b, 1994;

Boussafir and Lallier-Vergès, 1997; Cavelan et al., 2019b; Gelin et al., 1995; Tribovillard et al., 2001).

These studies have made a meticulous characterization of the palynofacies, the maceral and the OM

geochemical composition of the KCF in the studied area. All the KCF organic compounds identified

by these studies and their characteristics under SEM, TEM and reflected light microscopy are

summarized in Table 1. The relative quantities of each of these constituents in the studied sample were previously determined by Cavelan et al., (2019a) and presented in Table 1. Before this study, the different macerals present in the studied rock were identified under reflected light and UV excitation; the result is shown in Figure 1. For a more detailed description of palynofacies, maceral composition and the calculation of the abundance of each component, see Cavelan et al., (2019a).

Table 1. Summary of the origin and the main characteristics under reflected light microscopy, SEM and TEM of the organic components identified by previous works (Boussafir et al., 1995b, 1995a, 1994; Cavelan et al., 2019a; Tribovillard et al., 2001) in the studied area of the KCF and their relative abundance in OM of the studied sample (from Cavelan et al., 2019a). AOM: Amorphous Organic Matter. OM: Organic Matter.

Palynofacies (transmitted light microscopy)	Corresponding macerals under reflected light microscopy and UV excitation	Origin	SEM description	TEM description	Abundance in the sample (%)
Orange AOM (orange gel-like homogeneous particles)	Thick laminar bodies, often called 'Bituminite'. Low brown fluorescence Often associated with pyrite.	Natural sulfurization of oil-prone phytoplanktonic lipidic fractions	Thick laminar homogeneous particles embedding minerals and pyrite framboids	Large homogeneous areas with a strong electron contrast and a nanoscopically amorphous texture with no apparent structure	42.5
Brown AOM (brown heterogeneous flakes)	Does not correspond to any recognizable maceral. OM dispersed in the mineral matrix. Responsible for the high fluorescence of the mineral matrix	Selective preservation of cell walls of microalgae	Small diffuse AOM domains mixed with clay minerals	Laminar structures (ultralaminae), sometimes elongated with a regular thickness	34
Black AOM (opaque aggregates)	Does not correspond to any recognizable macerals, OM dispersed in the mineral matrix	Mix of bacterial macromolecules with altered lignaceous debris	Diffuse OM mixed with woody fragments and minerals	Diffuse nanoscopically amorphous OM forming a continuous network around numerous imprints of minerals eliminated via acid treatments.	3.6
Various debris of plant tissue	Grey-reflective fragments of non-fluorescent inertinite and low grey-reflective debris of vitrinite	Fragments derived from the terrestrial biomass	Structured woody fragments with sharp edges, angular and arcuate shapes inherited from cell structures	Structured components with, sometimes, a 'shredded' texture.	14.8
Algal debris	Bright yellow-fluorescent Tasmanaceae bodies and brightly yellowish-fluorescent lamellar masses or elongated alginite bodies	Fragments derived from algae	Thin, elongated homogeneous amorphous particles	Alginite: nanoscopically amorphous structure with small sizes and filamentous forms. Tasmanaceae: thick walls of spores.	5.1

Significant variations of the content of these organic components exist in the studied KCF series (Boussafir and Lallier-Vergès, 1997; Herbin et al., 1995; Lallier-Vergès et al., 1995). The studied sample was selected to contain a relatively high total organic carbon content (TOC = 10.3 wt.%, Hydrogen index= 557 mg HC/g TOC, Cavelan et al., 2019a) and high contents of brown and orange AOM, which are the predominant OM components in the KCF.
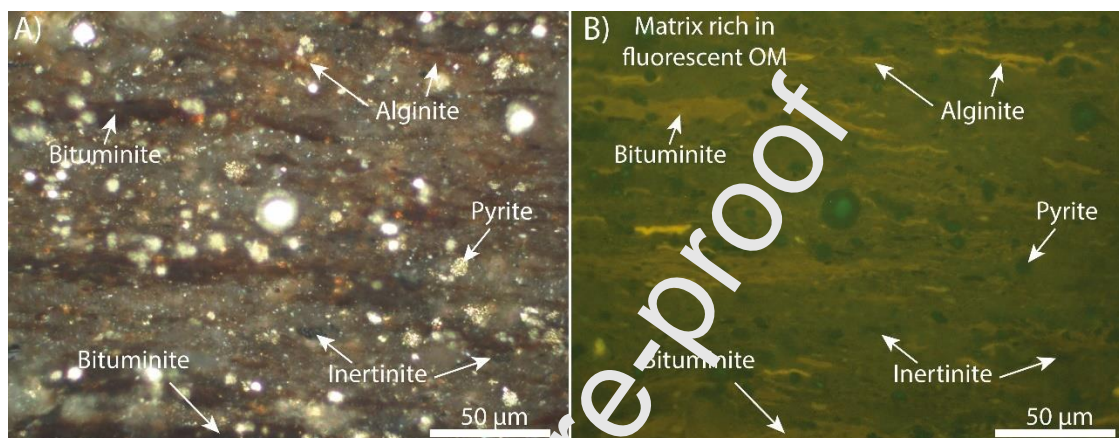

Figure 1. A) Photomicrographs showing the typical maceral composition of the studied sample before thermal maturation. Observations were carried out under oil immersion and reflected light using a Leica® DMRX microscope. B) Same field as A) under UV-fluorescence illumination.

Note that for the rest of the manuscript, the terms from palynofacies observations (orange, brown and black amorphous organic matter (AOM) are used to refer to the corresponding OM compounds rather than those from the maceral composition (such as Bituminite) because some of these OM compounds are diffused in the mineral matrix and do not correspond to any macerals (i.e black and brown AOM) that could be named.

2.2. Thermal maturation experiments

About 5g of the total rock sample was crushed into powder (< 250 μm) and sealed under argon atmosphere inside five separate gold cells (L = 6.5 cm, i.d = 0.5 cm, wall thickness 0.45 mm). The cells were introduced into high-pressure stainless-steel autoclaves. A constant hydrostatic external

pressure of 600 bars was exerted on the sample during the experiments. For more details, see Cavelan et al. (2019). The samples were heated under isothermal conditions at temperatures ranging from 325 - 470°C for 72 hours. The temperature of the system was raised at 4.5°C min^{-1} to the final temperature. Thermal maturations were conducted simultaneously on small-diameter rock cylinders (5 mm in diameter; 1.5 cm in length, drilled perpendicular to the bedding) to prepare polished sections for vitrinite reflectance measurements.

2.3. Vitrinite reflectance

Mean vitrinite reflectance (Ro) was measured on bulk rock polished sections made from immature and artificially matured rock cylinders of the sample impregnated with epoxy resin. The bulk rock sections were prepared using mechanical polishing perpendicular to bedding (abrasive grinding paper up to P4000 and alumina polishing suspensions up to 0.04 μm). For each measurement, between 50 and 60 random measurements were carried out on the same polished rock sections using a microscope equipped with a photometer and an oil-immersion objective (Leica® DMRX microscope) calibrated with glass-reflectance standards (Bertrand et al., 1993; Robert, 1971).

2.4. Nitrogen adsorption measurements

Immature and artificially matured samples were crushed into powder (<250 μm). Low-pressure nitrogen adsorption measurements were carried out at 77K on a Quantachrome® NOVA 2200^e apparatus to measure the total rock pore volume before and after maturation. These analyses were done on total rocks before the extraction of the extractible OM (oil and bitumen) and before the isolation of the OM. Before analysis, about 1 g of sample was outgassed for 24h under vacuum at 105 °C. The isotherms were obtained under the relative pressure P/Po ranging from 0.003 to ca. 0.99 with an equilibration time of 100 s. The pore volume was determined at the relative pressure P/Po of 0.99.

2.5. OM isolation

The bitumen fraction of immature and artificially matured rocks was ultrasonically extracted with a mixture of dichloromethane/methanol (1/1, v/v). For the geochemical analysis, see Cavelan et al., (2020). The residual OM was isolated by a fluoridric/hydrochloric acid treatment. Raman spectroscopy, SAXS, SEM and TEM observations were carried out from these isolated OM residues.

2.6. Raman spectroscopy

Raman spectroscopy was performed on the isolated OM samples using a confocal Raman Renishaw® InVia Reflex micro-spectrometer to assess the kerogen chemical structure. A 514.5 nm argon laser focused by a Leica® DM2500 microscope with a 100× magnification objective was used as the light source. The intensity of the laser power was set at 0.1% (=0.05 mW). Data were collected over the first order Raman spectrum (700 to 2300 cm^{-1}). For these analyses, the isolated OM powders were past on slides without any other preparation. For each sample, eight measurements were performed on randomly selected areas on all the sample surface to ensure reproducibility of measurements and estimate standard errors. Each spectrum is the average of at least 10 scans. The Raman spectra were analyzed using PeakFit software. According to Schito et al. (2017), the curve fitting and the deconvolution of bands were performed using mixed Gaussian-Lorentzian band profiles applied to six peaks and using a linear baseline. The calibration curve of Sauerer et al. (2017) between the Raman Band Separation (RBS) calculated from the measured G and D1 Raman band positions and the vitrinite reflectance of Type II organic-rich mudstones served to estimate the Raman vitrinite reflectance equivalence (Req) of artificially matured KCF isolated OM.

2.7. SEM

SEM observations were conducted using secondary electron (SE) modes using a SEM Merlin Zeiss®

equipped with an in-lens secondary electron at a working distance of 7.7 mm at 13 kV. Identification

of macerals in SEM images was possible by comparison with the organic compounds previously

identified during conventional petrographic observations (Figure 1). The isolated kerogen powder was

fixed to SEM stubs with a copper paste and coated with carbon without any other preparation.

2.8. TEM observations

TEM observations were performed under 200 kV using a Philips CM20 Transmission Electron

Microscope, equipped with a LaB6 filament and an EDX detector to show the evolution of the OM

texture with increasing maturity. The observations were conducted on ultrathin sections prepared from

the isolated OM according to Boussafir et al. (1995b, 1994). The OM was fixed in osmium tetroxide,

embedded in resin and cut in ultrathin sections using an ultramicrotome and placed on copper TEM

grids before the observations. The identification of macerals in TEM images was carried out by

comparison with the organic compounds identified during conventional petrographic observations

(Figure 1) carried out on the same KCF sample series (Boussafir et al., 1995b, 1994).

2.9. SAXS

SAXS measurements were performed on the isolated OM before and after thermal maturation and

after the extraction of the extractible OM using a Xeuss 2.0 SAXS system (XENOCS company) at the

Interface Confinement Materials Nanostructure laboratory (ICMN). SAXS and WAXS data were

collected simultaneously. For SAXS measurements, the sample-detector distance was configured to

cover the continuous size range 0,5-80 nm. WAXS data were intercepted in the 2θ range 18-46°, i.e.

bragg distance in the range 0.2-0.5 nm. Samples were placed inside 1mm diameter borosilicate glass

capillary. 1D scattering profiles I(q) were corrected for empty capillary scattering, transmission and

the incident X-ray flux density. The scattering intensity was corrected in assuming a pore-matter system and the porosity (P), the specific surface area (Sv), and the mean chord in pores ($\overline{l_p}$, mean pore size in nm) were calculated from the scattering power Q according to Cohaut et al. (2000).

2.10. Elemental analyses

Elemental analyses (C, H, N, S) were carried out on the isolated OM using a Thermo Scientific Flash 2000 organic analyzer on three replicates and assuming an analytical error of ±0.05 %. The oxygen content was graphically determined using the Van Krevelen diagram from H/C and mean vitrinite reflectance values. The content of sulfur includes both the sulfur of OM and pyrite.

3. Results

3.1. Elemental composition and Raman spectroscopy

The elemental composition of the isolated OM of KCF samples before and after thermal maturation is presented in Table 1. Carbon is largely predominant. The hydrogen and oxygen contents decrease with the increase in thermal maturity while the number of carbon and nitrogen atoms remains relatively constant. The H/C atomic ratio decreases from 1.29 to ~0.30 during maturation (Figure 2). A slight shift is observed between our artificial thermal maturations and the trend of natural environments (Figure 2). While the amount of hydrogen of our artificially matured OM follows the trend observed for natural Type II kerogen during thermal maturation, the amount of oxygen decreases more slowly after heating at 325°C and 350°C than expected in the Van Krevelen diagram.

Table 1. Elemental composition (wt.%) normalized to 100%, H/C and O/C atomic ratios of KCF isolated OM before (initial) and after maturation at 325-470°C for 72 hours.

Sample	N	C	H	S[a]	O	H/C	O/C
Immature/initial	4.61	66.76	7.19	8.97	12.46	1.29	0.14
325°C	4.29	71.93	4.89	9.30	9.57	0.82	0.10

350°C	4.93	71.27	4.46	11.41	7.93	0.75	0.08
390°C	5.14	79.36	3.00	7.00	5.50	0.45	0.05
440°C	5.42	83.65	2.91	3.44	4.57	0.42	0.04
440°C	5.01	84.34	2.04	5.57	3.04	0.29	0.03

^aThese data include the sulfur of pyrite closely associated with the OM.
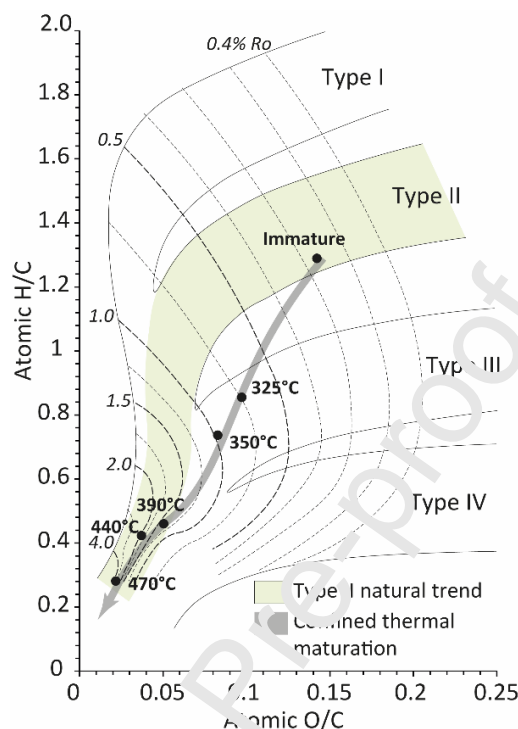
Figure 2. Evolution of H/C and O/C atomic ratios with increasing maturation temperature.

All the samples exhibit clean first order Raman spectra which consist of the two main bands characteristic of kerogen, G (~1600 cm^{-1}) and D (~1350 cm^{-1}, Figure 3). The initial immature samples exhibit, however a poorer signal-to-noise ratio. The G band, often called 'graphite band' is known to correspond to well-ordered graphite-like carbon structures and results more specifically from the longitudinal stretching vibration mode (E_{2G2} vibrational modes) of the C=C bond (sp^2 carbon) of well-structured aromatic rings with a D^4_{6h} symmetry (Tuinstra and Koenig, 1970). A D2 band is sometimes present as a shoulder to the G band, but it was often impossible to clearly separate the two components in our samples. G and D2 bands were thus considered as one broad band. The global D band (~1350 cm^{-1}) is generally assigned to discontinuities/ structural disorders of the kerogen sp^2 carbon network

(Tuinstra and Koenig, 1970). Mernagh et al. (1984) and Beyssac et al. (2002) suggested that these defects result from specific in-plane vibrations of heteroatoms (H, O, N and S) or C=C groups present at the edge. According to the best fit (using only Lorentzian curves), the Raman spectra were deconvoluted into 6 peaks (Figure 4).
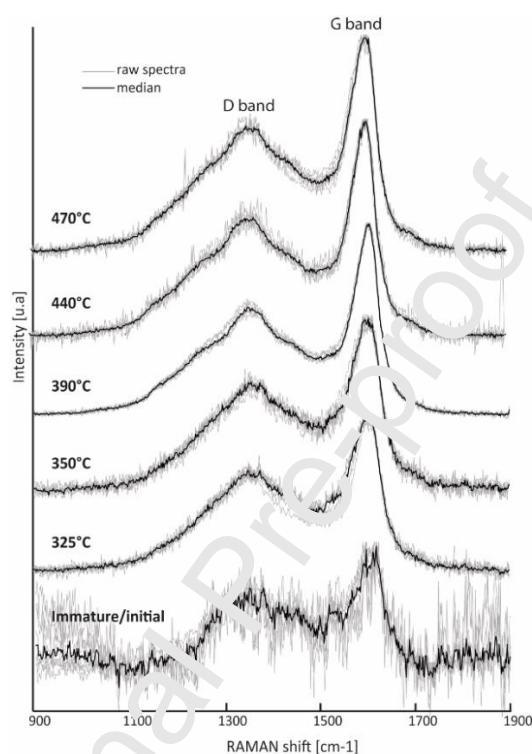

Figure 3. Measured Raman spectra of KCF isolated OM at different thermal maturity and position of D and G bands. The spectra are offset for clarity. Light grey: superposition of the different raw spectra of each sample. Black: median spectrum.
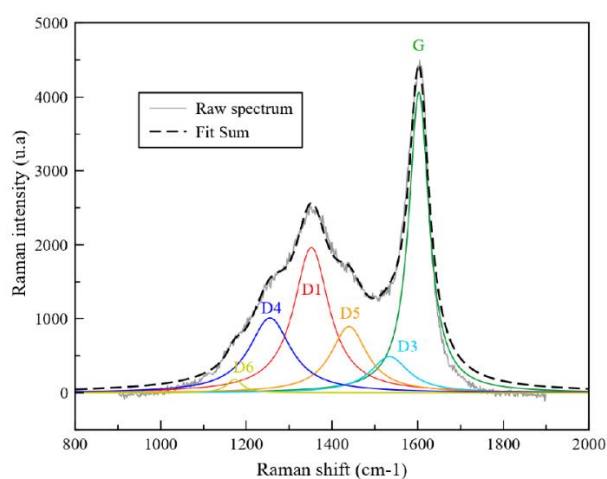
Figure 4. Spectral deconvolution and identification of the main Raman bands after maturation at 440°C.

Table 2. Position and the chemical functional groups correspondence of each Raman band after Lin-Vien et al. (1991), Sadezky et al. (2005), Li et al. (2006), Rebelo et al., (2016) and Schito et al., 2017.

Band name	Mean position (cm-1)	Description
D6	~1185	C-C and C-H on aromatic rings; C aromatic - C alkyl in aromatic or aliphatic ethers.
D4	~1240	Para-aromatics; Aryl–alkyl ether.
D1	~1380	Amorphous carbon structures; methyl group; aromatic rings.
D5	~1450	Amorphous carbon structures; methyl or methylene groups, aromatic rings.
D3	~1540	Amorphous carbon structures; poly-aromatics with 3-5 rings or polyacetylene-like structures
G	~1590	Alkene C=C; aromatic ring; ideal graphitic lattice.

The 'D band region' can be divided into a central D1 band (~1380 cm^{-1}) and three satellite bands: D4 (~1240 cm^{-1}), D5 (~1450 cm^{-1}) and D6 (~1185 cm^{-1}) commonly observed (Li et al., 2006; Lin-Vien et al., 1991; Sadezky et al., 2005) also in mudstone reservoirs (Liu et al., 2017). The 'G band region' can be divided into two bands: G (~1590 cm^{-1}) and D3 (~1540 cm^{-1}) which corresponds to the overlap between global G and D bands (Figure 4). Each of these bands was assigned to the chemical functional groups summarized in Table 2 and referenced in Sadezky et al. (2005) and Li et al. (2006). D3, D4, D5 and D6 bands, sometimes called Gr, Dl, Dr and S respectively (Rebelo et al., 2016; Schito et al., 2017), are thus associated with the presence of low-size aromatic domains exhibiting structures analogous to those of polyaromatic hydrocarbons (Li et al., 2006; Rebelo et al., 2016; Schito et al., 2017).

During thermal maturation, the raw D band positions are progressively shifted from ~1382 cm^{-1} to ~1349 cm^{-1} (Table 3). The G position decreases to ~1596 cm^{-1} after heating at 325°C and then re-increases progressively to ~1604 cm^{-1} after maturation at 350°C to 470°C for 72 hours. This variation of raw D and G positions results from a progressive increase in the Raman band separation (RBS)

from 224 to 254 cm^{-1} (Table 4). Note, however, that the D and G positions exhibit a great variability

within different organic particles of the same sample at the origin of the variability of the RBS (Table

4).

Table 4. Main median Raman parameters of KCF isolated OM including raw D and G band positions

(D_{pos} and G_{pos}) and intensity (D_{int} and G_{int}), D_{int}/G_{int}, D_{area}/G_{area}, Raman band separation (RBS= G_{pos}-

D_{pos}), Raman calculated vitrinite reflectance (Req), mean vitrinite reflectance (Ro), G and D full width

at half maximum (FWHM G and FWHM D).

Sample	D_{pos} (cm^{-1})	G_{pos} (cm^{-1})	RBS (cm^{-1})	Sd.	Req[a] (%)	Sd	Ro[b] (%)	Sd	D_{area}/G_{area}	D_{int}/G_{int}	FWHM G (cm-1)	FWHM D (cm-1)
Initial	1382	1607	224	±3.8	0.50	±0.09	0.42	0.03	2.2	0.9	39	87
325°C	1361	1596	235	±3.6	0.86	±0.17	0.72	0.04	2.0	0.7	36	99
350°C	1360	1596	238	±2.7	1.00	±0.14	0.90	0.05	1.8	0.7	34	102
390°C	1353	1599	245	±1.3	1.50	±0.10	1.39	0.04	1.9	0.6	27	107
440°C	1355	1604	248	±2.4	1.70	±0.23	1.82	0.06	1.6	0.6	27	107
470°C	1349	1604	254	±3.8	2.30	±0.44	2.12	0.10	1.5	0.5	24	108

[a]*Req: equivalent vitrinite reflectance calculated using the RBS parameter from the data of Cheshire et al. (2017). Req= $4.10^{-6}.exp(0.0523*RBS)$. Sd: Standard deviation.* [b]*Ro: Mean vitrinite reflectance.*

The reference calibration curve from Sauerer et al. (2017) (in blue, Figure 5) was thus used to estimate

the Raman vitrinite reflectance equivalence (Req) from the RBS of KCF samples (Table 4). The Req

values show a relatively high standard deviation due to the uncertainty of the G and D positions, even
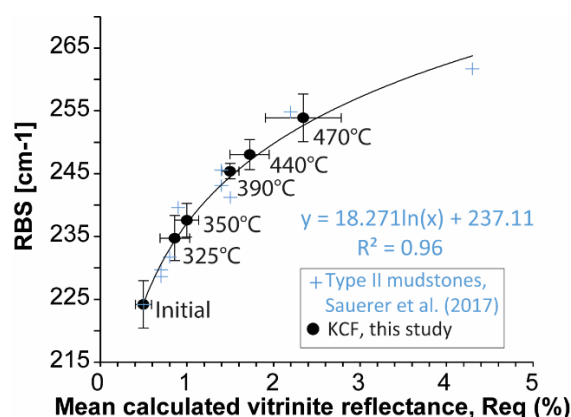
for the higher maturity stages (Table 4).

Figure 5. Comparison of Raman band separation (RBS) from artificially matured OM (this study) and organic-rich mudstones (Sauerer et al., 2017). This served to determine the equivalent vitrinite reflectance of our samples.
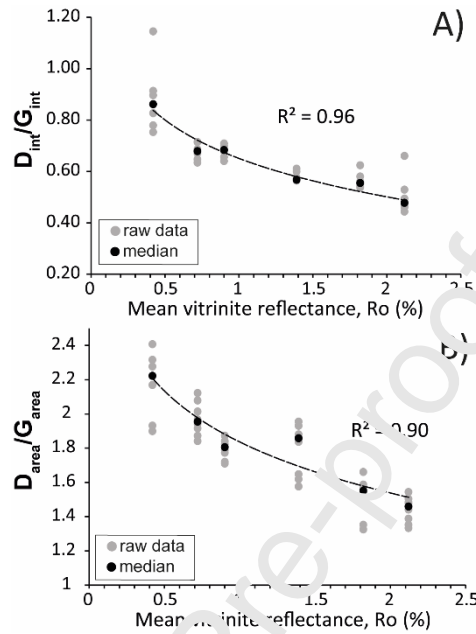

Figure 6. Evolution of A) D area/G area and B) D intensity/G intensity as a function of thermal maturity.
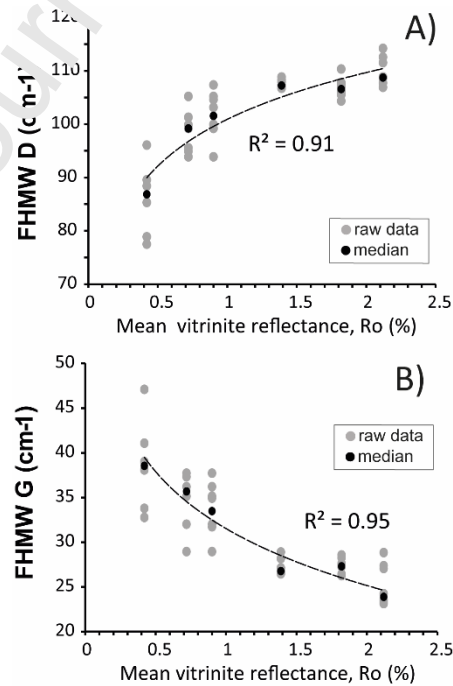
Figure 7. Evolution of A) D full width at half maximum (FWHM D) and B) G full width at half maximum (FWHM G) as a function of thermal maturity.

A relatively good correlation exists between the mean calculated vitrinite reflectance (Ro) and the equivalent vitrinite reflectance values determined using the RBS (Req, Table 4). Before maturation the Req of 0.50% ±0.09 and the Ro of 0.42 ±0.03 well corroborating the low maturity of the sample. After thermal maturation from 325°C to 470°C for 72 hours, Req increases from 0.86 ±0.17% to 2.34 ±0.44% and the Ro increases from 0.72 ±0.04% to 2.12 ±0.10% indicating that thermal maturity ranging from the oil generation to the dry gas zone have been reached. Meanwhile, the relative intensity of the raw G band increases while the intensity of D bands decreases (Table 4). Consequently, D_{area}/G_{area} and D_{int}/G_{int} ratios decrease progressively with increasing thermal maturity (Table 4, Figure 6A, B). The full width at half maximum (FWHM) of the G band decreases with increasing thermal maturity while the FWHM of the D band increases (Figure 7A, B).

3.2. SEM and TEM residual OM texture observations

In SEM images (SE), OM appears initially as amorphous OM (AOM) particles (Figure 8A, B). These components exhibit no distinct shape or structure and have a homogeneous texture at the observation scale (Figure 8A). Some of these particles present distinct edges and are closely associated with pyrite framboids (Figure 8E) or contain inclusions of isolated pyrite grains (Figure 8A) (confirmed by EDX analyses). The other part of the amorphous OM appears as an agglomeration of various AOM particles without any distinct edges or shapes (Figure 8B) probably stacked together after the dissolution of the mineral matrix by the acidic treatment. This AOM is accompanied by various structured components (Figure 9A, B). These particles of various sizes contain sharp edges and distinct arcuate shapes probably inherited from cellular structures (Figure 9B). The surface texture of most these particles is

relatively homogenous at the observation scale. Some of these fragments contain, however large macropores probably inherited from the cellular structure. The inertinite like fragments exhibit no variation of texture at the micrometric scale during maturation (Figure 9C, D). Their arcuate shapes and cellular structure are still visible during dry gas generation and their surface texture still appears homogeneous. Contrary to these structured fragments, the texture of the AOM shows significant changes with increasing thermal maturity (Figure 8C-E).

In the early oil generation stages (Ro= 0.72%, 325°C/72 hours), no real changes in the surface texture of OM are observed. The AOM still mainly exhibits a homogeneous microtexture. Locally, some amorphous OM aggregates present nevertheless a slightly granular texture, not observed in the immature sample (Figure 8C). In the condensate wet gas zone (Ro= 1.39%, 390°C/72h), most of the AOM exhibits an irregular and granular surface texture at the micrometric scale (Figure 8D). In the dry gas zone (Ro =2.12, 470°C/72h), the OM surface texture is highly heterogeneous (Figure 8E). OM occurs mainly as an agglomeration of small spherical OM grains, less than 100 nm in diameter, stacked together and mixed with pyrite framboids (confirmed by EDX analyses, Figure 8F). Pyrite framboids remain abundant in the dry gas zone and do not appear to be affected by thermal maturation (Figure 9F).

In TEM observations different organic structures are present. No real differences are observed between the immature stage and the early oil generation stage (Figure 10). Before thermal maturation (Ro=0.42%), the OM is mainly composed of a diffuse organic material (light grey material widespread between imprints of minerals (white) dissolved by the acidic treatment, Figure 10A, B). These areas contain different thin elongated particles (orange arrows, Figure 10B) whose edges are often difficult to identify. In these areas, the OM exhibits an amorphous structure (Figure 10A, B). Various

structured components are observed (Figure 10E, 11A, E). In our TEM images, they often exhibit a 'scaly' or a 'shredded' heterogeneous texture (Figures 10E, 11A, E). The 'scaly' texture of these particles shows parallel scratches which are probably artefacts created by the diamond knife during the cutting of ultrathin sections. Some of particles show elongated shapes, rounded ends, a width of ≈700 µm and irregular surface texture (Figure 10C, D).
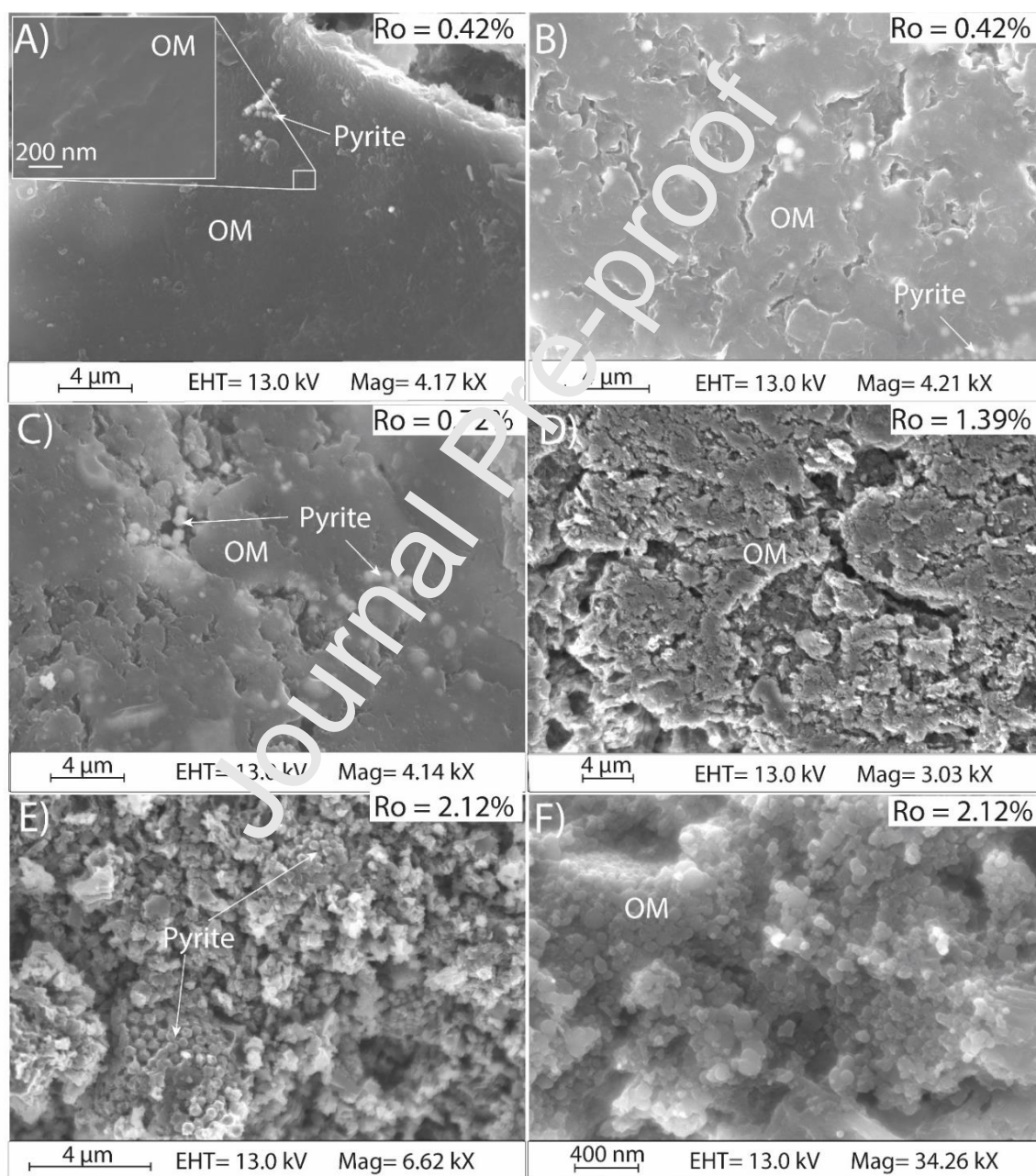
Figure 8. A-D) SEM images (SE) showing the evolution of the texture of the isolated organic matter (OM) with increasing maturity. A) The large geometric pores are the imprint of minerals dissolved during acidic treatment. B) Agglomeration of various amorphous particles. C-E) Agglomeration of various amorphous particles with an increasingly heterogeneous granular texture. F) Zoom on the granular OM of overmature samples. Ro: mean vitrinite reflectance. The presence of pyrite was confirmed by EDX analyses.
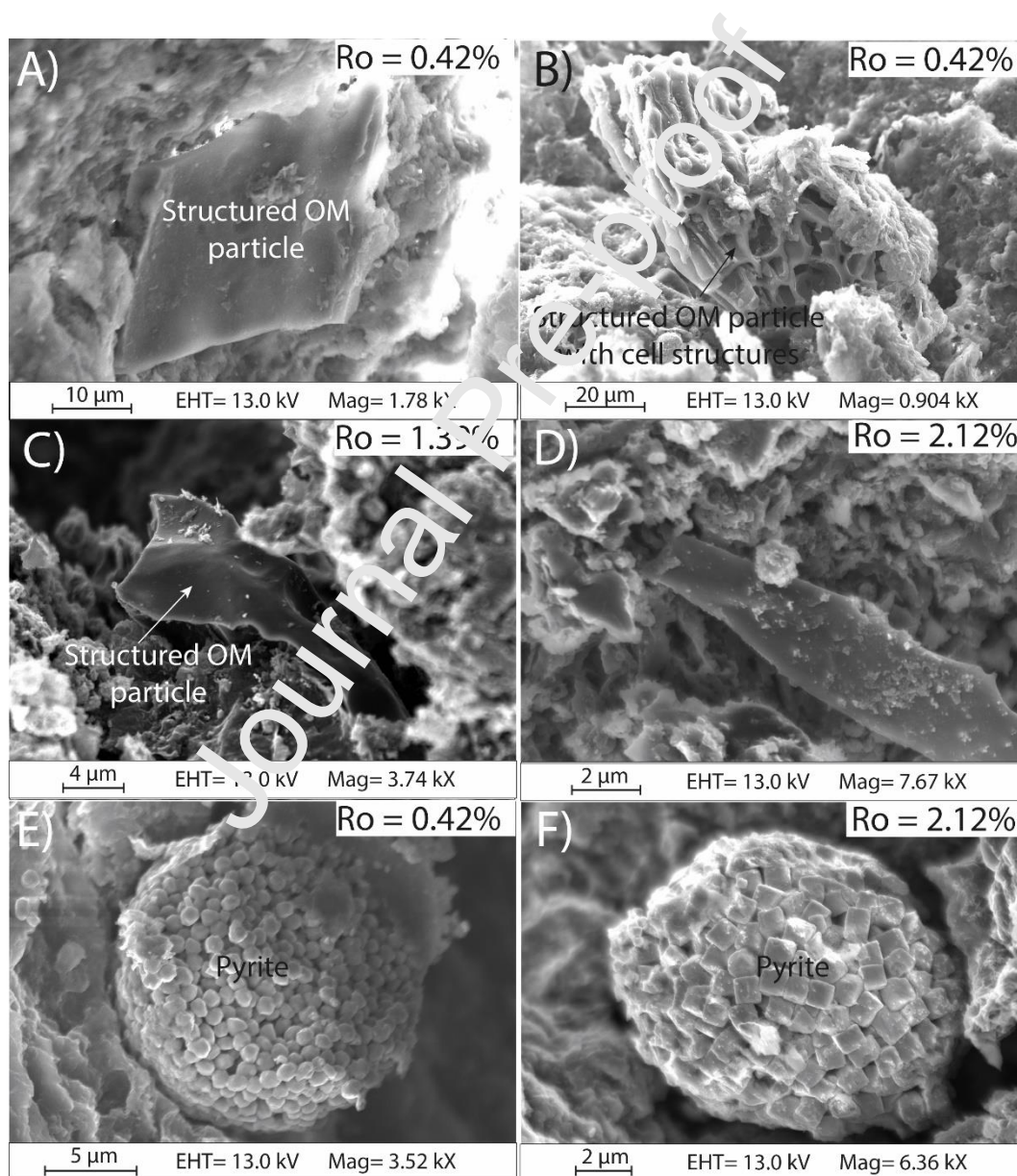
Figure 9. A-D) SEM images (SE) of various fragments of structured OM particles observed at different thermal maturity stages. E-F) Example of pyrite framboids observed for all maturity stages. The presence of pyrite was confirmed by EDX analyses. Ro: Mean vitrinite reflectance.
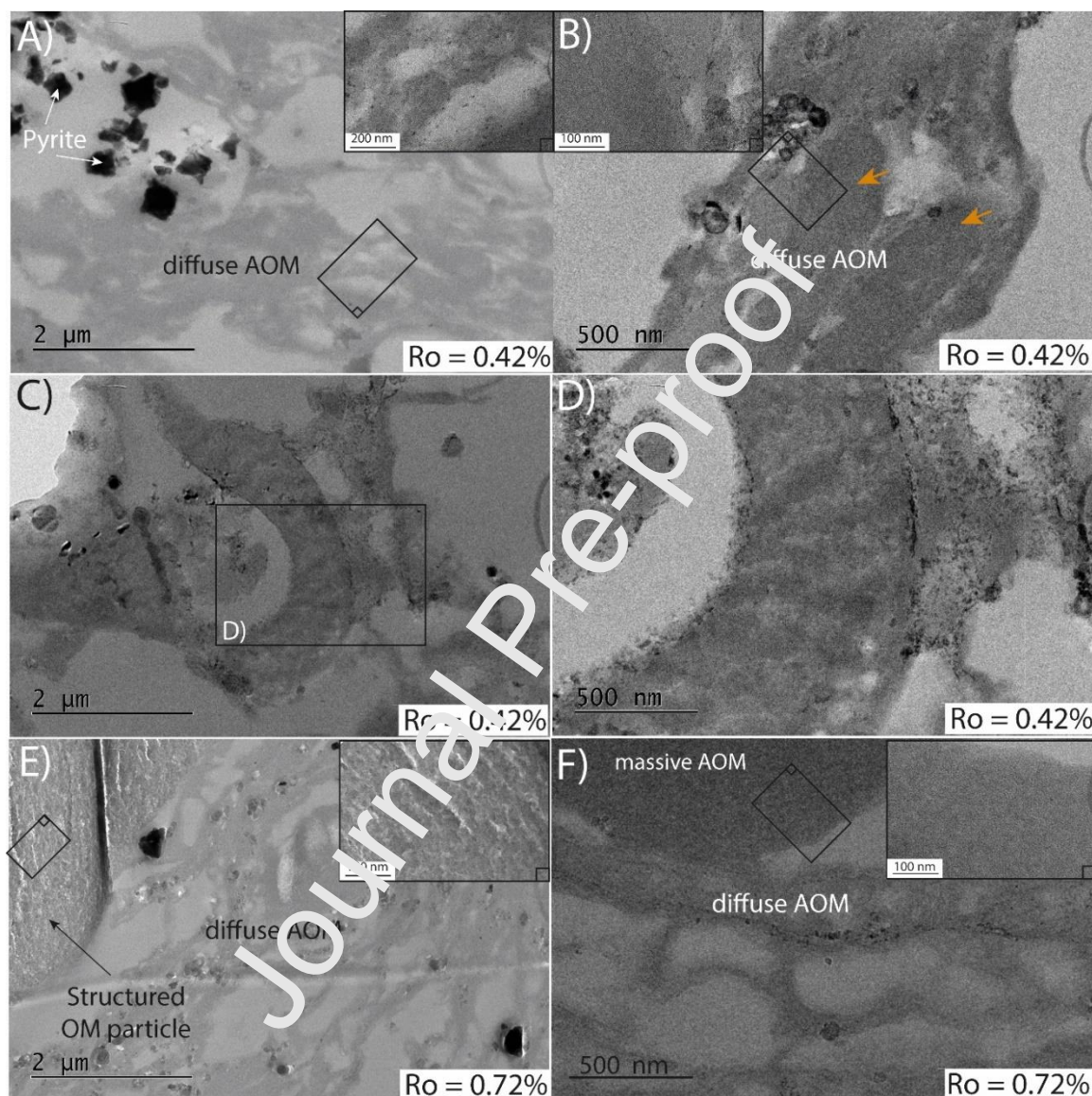

Figure 10. TEM observation of various organic components of the isolated OM of immature KCF samples. A-B) Diffuse amorphous OM (AOM) between imprints of dissolved minerals (white) and isolated pyrite grains in immature kerogen (confirmed by EDX analyses). Orange arrows show different elongated amorphous particles in diffuse amorphous OM areas. C-D) Elongated structured components with rounded ends showing an irregular surface texture suggesting the possible presence

of nanopores. E) Diffuse AOM with fragments of a structured OM particle. F). Diffuse AOM with

near a more massive AOM particle. The black grains in the images are Osmium grains used to fix the

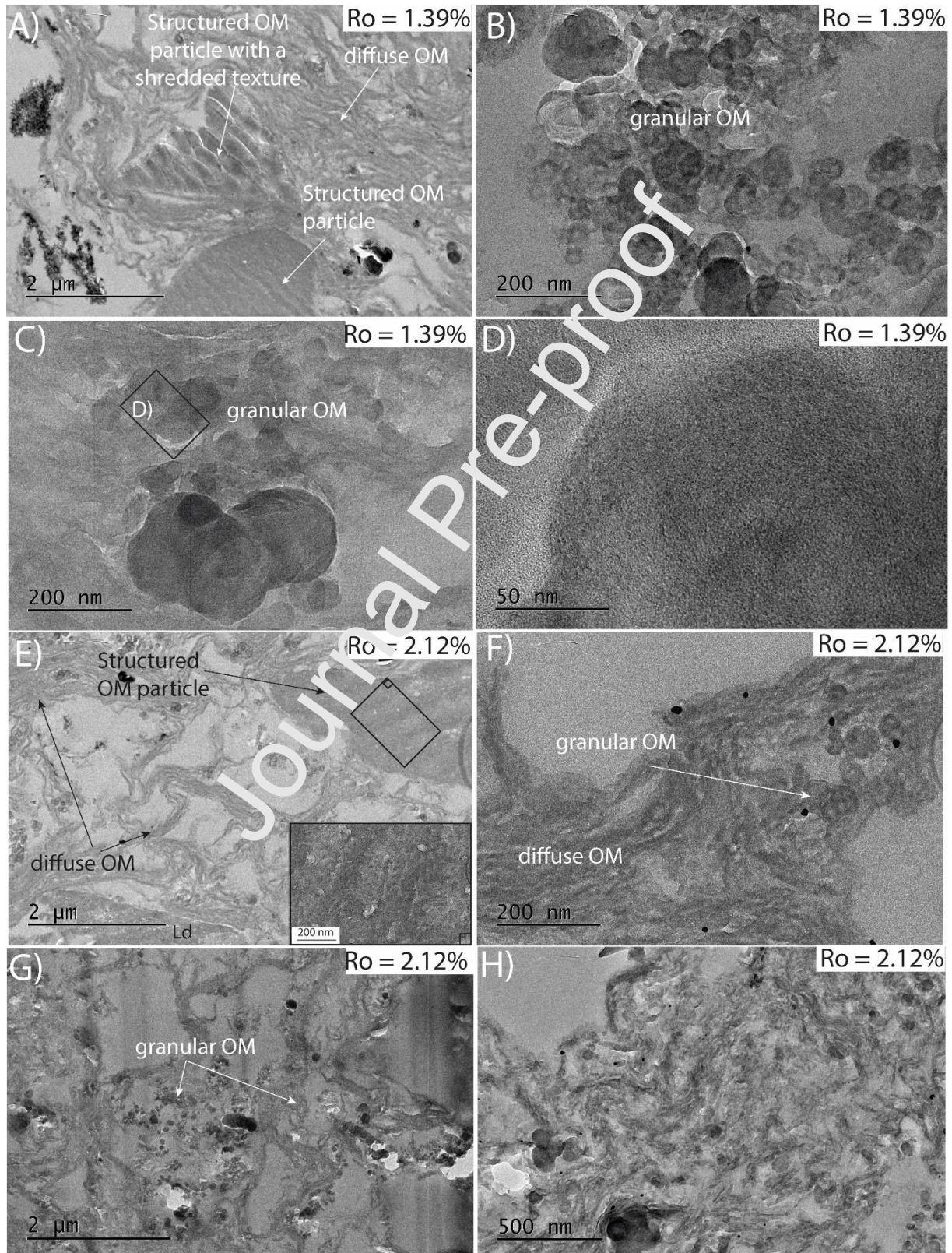OM. Ro: Mean vitrinite reflectance. The light grey areas are imprints of dissolved minerals.

Figure 11. TEM observations of organic components in isolated OM of thermally-mature KCF samples. A, E) Various fragments of structured OM particles. B-D, F-H) Granular OM particle. The light grey areas are imprints of dissolved minerals. Ro: Mean vitrinite reflectance.

This kind of particles is, however, relatively scarce. Locally, more massive (largest areas) amorphous OM particles without mineral imprints are present and exhibit a perfect amorphous texture at the observation scale (Figure 10F). Contrary to the diffuse AOM (Figure 10A), these massive particles have relatively distinct edges and exhibits a slightly higher contrast. After thermal maturation at 390°C (condensate wet gas zone, Ro= 1.39%) and 470°C (dry gas zone, Ro= 2.12%) for 72 hours, no variation in the texture of the structured compounds is visible at this nano-scale (Figure 11A, E). However, differences are observed for the diffuse and the massive amorphous OM (Figure 11). In the condensate wet gas zone, the OM appears locally as an agglomeration of small grains of OM whose size varies from 20 to 200 nm in diameter (Figure 11B-D). In the dry gas zone, these granular areas become more abundant (Figure 11E, G) and most of the OM particles exhibit a heterogeneous texture at the TEM observation scale (Figure 11F, H).

SAXS measurements

Figure 12 shows SAXS profiles of the isolated OM of KCF samples at different thermal maturities. Note that assuming a system composed of two homogeneous phases: the porosity hosted by the OM and the OM itself, the scattered intensity varies in $q^{-\alpha}$ with $\alpha= 4$ in the case of smooth interface (Porod law) leading to a slope = -4 in a log-log scale system. For our samples, the slope ranges between -3.7 to -3.8 due to the chemical heterogeneity of the OM. For $q<2$ nm^{-1} ($d_{bragg} > 4$ nm), the measured scattering intensity depends on the porosity but also on the variations in the electronic

density, which can occur in the pores hosted by the OM or in the OM itself, due either to the filling of

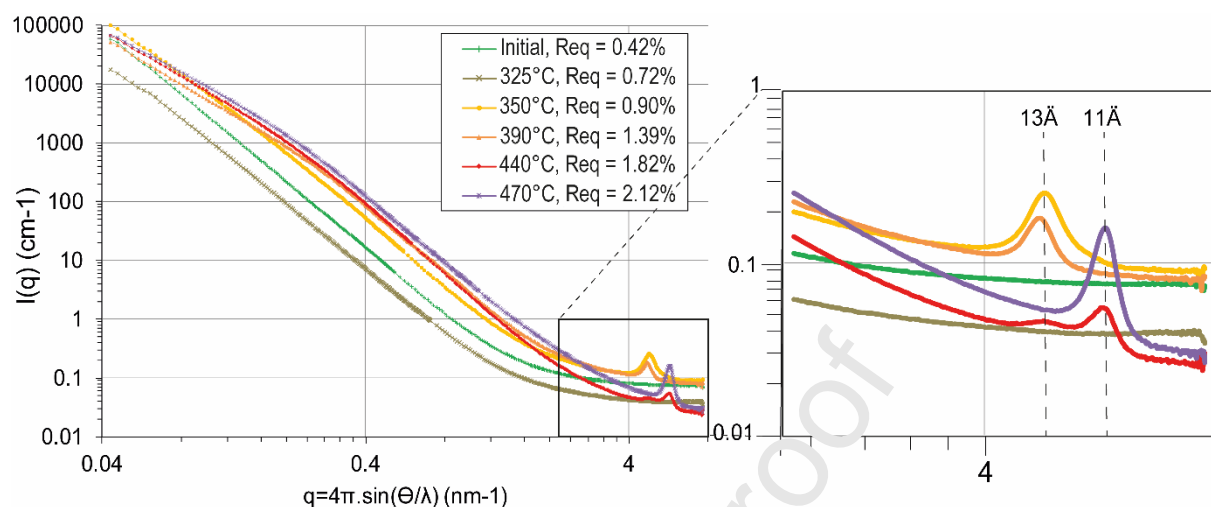pores by fluids or chemical heterogeneity of the OM during thermal maturation.

Figure 12. SAXS profiles of isolated OM before and after thermal maturation at 325°C to 470°C for

72 hours. I(q) is the scattering intensity. q is the magnitude of the scattering vector.

Variations in the shape of SAXS profiles are attributed to the change in the distribution of the porosity

in size and/or in quantity, whereas a change in the intensity of these curves without changes of shape

indicates a variation in the electronic contrast between OM and the OM-hosted pores. Firstly, after

maturation at 325°C for 72 hours, an overall decrease in the scattering intensity is observed without

any changes in the shape of the curves (Figure 12). This indicates a decrease in the overall electronic

contrast of the pore phase, probably filled with fluids. Above 325°C, the scattering power Q increases

with increasing thermal maturation temperature (Table 5). This is accompanied by a change in the

shape of the scattering intensity curves (Figure 12). This phenomenon suggests both an increase in the

electronic contrast due to the progressive organization of the OM in response to thermal maturation

and the development of pores in volume and size (open or not). Note that scattering intensities

continue to rise with decreasing q instead of reaching a constant value, suggesting that the size of one

of the homogeneous phases exceeds the lowest q-range of our measurements (size >80 nm) (Figure 12).

Table 5. SAXS parameters of OM including the scattering power Q, the matrix density ρ_m (pores excluded), the contrast term $\Delta\rho^2 = (\rho_m - \rho_{pores})^2$, the porosity P, the surface area S_{area}, the mean pore chord $\overline{l_p}$ (nm).

Sample	Immature/initial	325°C	350°C	390°C	440°C	470°C
Q (nm^{-3}.cm^{-1})	6.79	2.51	16.9	18.4	21.8	27.1
ρ_m (g.cm^{-3})	0.65	0.79	0.84	1.06	1.14	1.10
$\Delta\rho^2$	3.86	4.83	5.37	8.32	9.48	8.94
P	0.10	0.03	0.20	0.15	0.13	0.19
Sv (m².g^{-1})	16	5.34	37.6	46.5	39.7	57.1
$\overline{l_p}$ (nm)	24.8	20.3	21.2	14.1	13.2	13.3

For q > 7.5 nm^{-1}, modulations are observable in SAXS profiles from 350°C to 470°C around d= 1.3 nm and 1.1 nm (Figure 12). The modulations at 1.3 nm are present after maturation at 350°C, 390°C and 440°C for 72 hours. From 440°C this modulation is however less intense and disappears totally after heating at 470°C while the intensity of the modulation at 1.1 nm rises in intensity. The position of these reflections could be attributed to a dehydration of clay minerals with increasing temperature, embayed in the OM and thus protected from acidic treatment. However, these phases are not present for the immature and early mature samples (initial and 325°C, Figure 12). This is surprising if we assume that the irradiated volume is representative of the overall sample composition (including both OM and mineral), since we assume that all the studied samples exhibit similar mineralogy. These reflections may also be related to other mineral phases, not affected by acidic treatment, identified in the diffraction profiles at wide angle. Further investigations and especially replicates of these analyses are thus required to better understand these variations. The electronic contrast pore-OM ($\Delta\rho^2$), the porosity (P), the specific surface area (Sv) and the mean pore chord length ($\overline{l_p}$, mean pore size) calculated after the scattering power of samples are presented in Table 5 (see section I for the

expression of each parameter). According to SAXS profiles, the specific surface area, the porosity and

the mean pore chord decrease after heating at 325°C for 72h, suggesting the loss of pore volume

(Table 5, Figure 13). The specific surface area and the porosity develop at the same time from 350°C

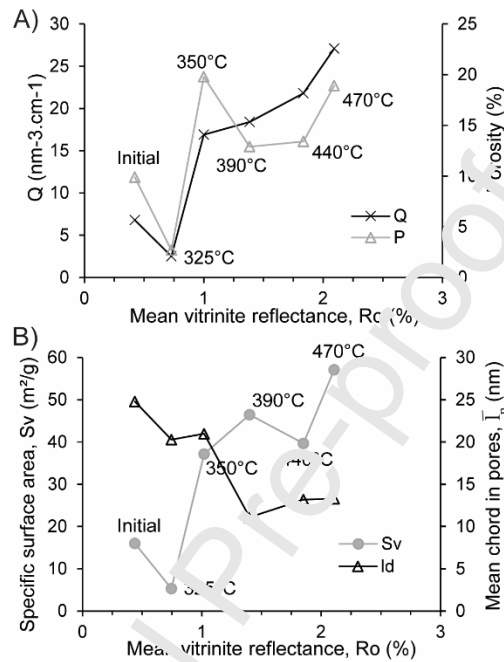to reach maximum values of about 57 m²/g and 20% respectively at 470°C.

Figure 13. Concomitant evolution of A) the scattering power Q, the porosity P, B) the specific surface

area Sv and the mean pore chord length $\bar{l}_p$ of the isolated OM of KCF samples with increasing

maturity.

The mean chord in pore decreases with increasing maturity to reach values ranging between 11.1 and

13.3 nm in diameter. Fluctuations in the porosity, the specific surface area and the mean pore size are,

however, observed from 350°C up to 470°C (Table 5, Figure 13) suggesting a non-linear increase of

porosity inside OM with increasing thermal maturity.

Total rock pore volume

The total rock pore volume measured by nitrogen adsorption measurements (before the

extraction of bitumen) varies between 5.10^{-3} and $8.2.10^{-2}$ cm³/g during thermal maturation (Figure 14).

Contrary to the OM porosity measured by SAXS, the pore volume decreases continuously from $3.6.10^{-2}$ cm^3/g to 5.10^{-3} cm^3/g after maturation at 325°C-350°C for 72 hours (Ro=0.72-0.90%). The pore volume is higher after maturation at 390°C ($4.0.10^{-2}$ cm^3/g) but decreases again after heating at 440°C for 72 hours. As for the OM porosity, a final increase of the pore volume to $8.2.10^{-2}$ cm^3/g is finally observed after maturation at 470°C (Figure 14).
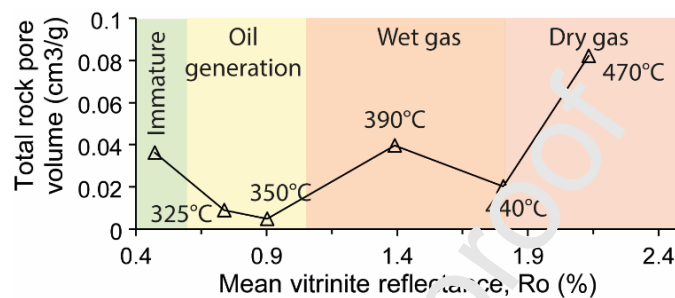

Figure 14. Evolution of the total rock pore volume measured by nitrogen adsorption during thermal maturation.

4. Discussion

4.1. Assessment of thermal maturity and OM structure evolution during thermal maturation using Raman spectroscopy

The first stage of thermal maturation is marked by the progressive breaking of some C-C bonds, leading to the elimination of functional groups, saturated cycles and chains. This results in the loss of the hydrogen-rich aliphatic carbon groups and N, S, O heteroatoms to yield bitumen, CO_2, N_2 and H_2S (Behar and Vandenbroucke, 1987; Peters et al., 2007; Tissot et al., 1987; Tissot and Welte, 1984). These processes leave behind a hydrogen-poor kerogen residue largely dominated by aromatic carbon structures and hydrogen-rich bitumen (Behar and Vandenbroucke, 1987; Peters et al., 2007; Tissot et al., 1987; Tissot and Welte, 1984). In higher thermal maturities, the secondary cracking of residual

bitumen and kerogen leads to the progressive aromatization of the carbon-rich residue. In our samples, this is marked by the strong decrease in the H/C atomic ratio and H and S contents (Table 2, Figure 2).

Raman spectroscopy provides useful specific information about the molecular vibrations of specific chemical bonds (Table 3) (Beyssac et al., 2002; Li et al., 2006; Lin-Vien et al., 1991; Rebelo et al., 2016; Sadezky et al., 2005; Schito et al., 2017). We observed a good correlation between the Raman parameters investigated and thermal maturity of KCF isolated OM (Figures 5, 6, 7). According to previous work (Cheshire et al., 2017; Sauerer et al., 2017; Schito et al., 2017), RBS, G band FWHM, D_{int}/G_{int} and D_{area}/G_{area} are the Raman parameters that show the best correlation with maturity in the KCF ($R^2 > 0.90$, Figures 5, 6, 7). In previous works (Li et al., 2006; Schito et al., 2017), the decrease in G band intensity and FWHM with increasing thermal maturity was considered to be mainly due to the progressive disappearance of the D3 band (often called Dl band) which marks the decrease of the polyacetylene-like structures and/or the small aromatic carbon rings (3-5 benzene rings) in amorphous carbon structures (Rebelo et al., 2016). The progressive decrease of D_{int}/G_{int} and D_{area}/G_{area} (Table 4, Figure 6) is often attributed to the thinning of the G band in response to the clustering of the aromatic rings and the ensuing decrease in H, N, S and O heteroatoms leading to a concomitant decrease in D2, D4, D5, D3 and D1 bands (Ferrari and Robertson, 2000; Li et al., 2006; Tuinstra and Koenig, 1970). Meanwhile, the shift of the raw D band position to a lower wavenumber and the ensuing progressive increase in the RBS (Table 4, Figure 5) are known to result from the progressive increase in the number of larger aromatic domains (Ferrari and Robertson, 2000). This substantiates the normal progressive aromatization of KCF OM and its transition from disordered to more ordered carbon materials with increasing thermal maturity as observed in sedimentary basins with increasing burial. As previously observed for different types of OM (Cheshire et al., 2017; Ferrari

and Robertson, 2000; Quirico et al., 2005; Sauerer et al., 2017; Schito et al., 2017), the progressive

increase in the RBS seems to be driven by the shift of the D position while no clear variations are

observed for the G band position (Table 4).

According to previous studies (Beyssac et al., 2002; Cheshire et al., 2017; Liu et al., 2013;

Sauerer et al., 2017; Schito et al., 2017), the RBS appears to be a good parameter to estimate the

equivalent vitrinite reflectance of OM with mean vitrinite reflectance ranging between 0.4 and 2.4%.

A good correlation exists between the RBS of our artificially-matured samples and that of the organic-

rich marine mudstones from Sauerer et al. (2017) (Figure 5). Hence, the correlation of Sauerer et al.

(2017) between Rm and RBS was used to estimate the mean Raman vitrinite reflectance (Req) of KCF

OM with increasing thermal maturity. Although there are some differences between each of these

ratios, the Req (this study) and the Ro (Table 4). However, the error attached to these Req values,

generally slightly greater than the Ro standard deviations, is significant and does not allow a precise

estimation of thermal maturity (Table 4). This variability, also visible for all the Raman parameters

investigated (Figures 5, 6, 7), may be due to internal variations in the KCF kerogen chemical structure

and composition, which is initially composed of various particles of different origins and chemical

compositions (Table 1, Figure 1). Although the thermal cracking of kerogen and its aromatization

during thermal maturation progressively blurs the difference of chemical composition between

kerogen particles, this variability remains relatively high during thermal maturity stages. Although

easy to determine, these results suggest that thermal maturity from Raman spectroscopy should be

used with caution or in association with other maturity indicators for a precise estimation of vitrinite

reflectance.

4.2. Concomitant evolution of the texture, the structure and porosity of KCF isolated OM with increasing thermal maturity

4.2.1. Initial OM texture from the micro- to the nano-scale

As previously observed in the bulk rock polished sections (Cavelan et al., 2019a), SEM and TEM images of the isolated OM before maturation show that the OM is mainly composed of amorphous particles with a relatively homogeneous texture (Figures 8A, 10A-D). This is in accordance with previous SEM, TEM and conventional petrographic observations of immature KCF mudstones (Boussafir et al., 1995b, 1995a; Cavelan et al., 2019b). According to the observations of Boussafir et al., (1995b) (Table 1), the larger AOM particles in SEM, which often contain pyrite inclusions and distinct edges (Figure 8A) seems to correspond to the massive AOM particles observed in TEM (Figure 10F). These particles show a similar association with pyrite, a similar size and well-defined boundaries. According to Boussafir et al. (1995a), these particles may correspond to orange AOM (bituminite macerals, Figure 1), which are abundant in the studied sample (42.5 % of the OM, Table 1). The other part of the AOM is present as an agglomeration of different amorphous particles without distinct edges in SEM (Figure 8B), which likely corresponds to the diffuse AOM observed between mineral imprints in TEM (Figure 10A, B). Previous SEM and TEM investigations of Boussafir et al. (1995a), suggested that these particles are mainly composed of black AOM with a probable contribution of brown AOM. In view of the low black AOM content in these samples (3.6 % of the OM, Table 1) compared to brown AOM (36 % of the OM) and the abundance of these diffuse AOM particles in the studied sample, a strong contribution of brown AOM is, indeed, very likely. Diffuse (OM dispersed around mineral imprints with a low TEM electronic contrast) and massive (largest OM particles with no mineral imprints and a higher electronic contrast) AOM particles exhibit a

homogeneous amorphous texture from the micro- to the nano-scale. According to the maceral composition and previous petrographic observations (Table 1, Figure 1), the structured components could be identified as scarce lignaceous debris (Figure 9B) and various fragments of plant tissues (Figure 9A, inertinite like fragments). These particles are easily identifiable by their distinct structure and typical sharp edges (Guo et al., 2018; Milliken et al., 2013). Although most of these structured components exhibit a homogeneous surface texture in SEM (Figure 9A-D), some of these particles show a heterogeneous 'shredded' texture in TEM which may suggest the presence of primary nanopores (Figures 10C-E, 11A). Furthermore, the presence of large macropores inherited from the original biological structure of the organic components is sometimes visible in some lignaceous debris (Figure 9B). A contribution of these particles to the total porosity at the immature and low maturity stages (Ro ≤ 0.72%) cannot therefore be excluded. This probably explains the porosity of 10% measured on the isolated kerogen (Table 5). This provides support for previous observations made in various immature to early mature rocks (Ro ≈ 0.35-0.63 %) (Löhr et al., 2015; Reed, 2017) including the KCF (Katz and Arango, 2018) and clearly indicates that some specific structured organic compounds can contain primary OM-hosted pores inherited mainly from cellulose and woody fragments' cellular structures. Nevertheless, these lignaceous debris are relatively scarce in the studied samples, the contribution of their porosity to the total rock pore volume before and after thermal maturation is probably low, especially compared with the important porosity hosted by the mineral matrix (Cavelan et al., 2019b).

4.2.2. Evolution of the ultrafine structure of OM during oil and gas generation

The oil generation stage (325-350°C/72h, Ro=0.42-0.90%) is marked by a strong decrease in the kerogen H/C and S, O content due to the breaking of some C-C bonds of kerogen indicating the

thermal cracking of OM (Table 2). These processes mark a progressive structural change and aromatization of kerogen illustrated by a significant increase in the RBS, a decrease in the D_{int}/G_{int} and D_{area}/G_{area} (Figures 5, 6) and a densification of the kerogen structure (increase in the kerogen matrix density ρ_m, Table 5). In the early oil generation stage (Ro =0.72%), these processes have no impact on the OM surface texture at the micro- to the nano-scale (Figures 8C, 10E, F). In SEM and TEM, amorphous kerogen particles still appear amorphous and relatively homogeneous, no changes are observed for the structured components. This is well substantiated by SAXS measurements which reveal a densification of the isolated kerogen without any pore development. On the contrary, the decrease in the scattering intensity, the scattering power Q, the porosity P and the surface area suggest a significant loss of pore volume (Table 5, Figures 12, 13). This decrease in the isolated kerogen-hosted porosity coincides with the decrease in the total rock pore volume observed after heating at 325°C for 72 hours (Figure 14). According to SAXS profiles the variations of the isolated kerogen porosity are mainly due to the decrease in the overall electronic contrast between pores and OM. This may indicate a loss of the primary OM porosity by kerogen deformations during oil generation, such as swelling of kerogen by retained oil as described by Mathia et al. (2016) and recently observed by Ghanizadeh et al. (2020). The filling of part of the total rock pore volume by the bitumen and oil trapped in the porosity (not extracted before nitrogen adsorption measurements) may explain a great part of the total pore volume loss, (Figure 14), however, the OM porosity (SAXS porosity, P) was measured after the extraction of bitumen and oil by dichloromethane/methanol treatments. A filling of the isolate OM porosity by this extractible OM can thus not explain the decrease of the OM porosity after maturation at 325°C. These results reveal that the strong decrease in pore volume in the early oil generation stage observed in the total rock (Figure 14) or in KCF mudstones (Cavelan et al., 2019a) is

not only due to the filling of the interparticle pores associated with minerals by retained bitumen, but also due to a loss of the primary OM porosity. Note that the massive production of saturated and aromatic hydrocarbons after maturation at 325°C and 350°C for 72h of KCF samples was shown in previous geochemical investigations (Cavelan et al., 2020b). While the peak oil generation (350°C/72 hours, Ro=0.90%) corresponds to the loss of almost all the primary pore volume in total rocks (Figure 14), SAXS measurements show a strong increase in the isolated kerogen porosity marked by the concomitant rise of Q and porosity (Table 5, Figure 13). The specific surface area and the porosity of the OM increase strongly to 37.6 m².g^{-1} and 20%, respectively. The progressive densification and aromatization of the kerogen at this maturity stage seems to lead to a massive development of nanopores. The variations in both scattering intensity and curve shape in SAXS profiles show indeed the clear onset of the structuration of kerogen in two distinct phases: OM and pores from the peak of oil generation (350°C/72 hours, Figure 12). The mean pore chord length indicates the presence of mesopores (ca. 20 nm in diameter) (Table 5) but the still rising intensity with decreasing q in SAXS profiles indicates that larger pores, that exceed the lowest q-range of our measurements, are also present (Figure 12). These new results show that pores start to develop in KCF kerogen from the peak of oil generation, at Ro of ca. 0.90% in the KCF, and not only during gas generation and expulsion as previously suggested (Cavelan et al., 2019a). This substantiates previous observations which show the presence of pores in OM at vitrinite reflectance ranging from 0.80 to 0.90% in various organic-rich mudstones (Loucks et al., 2009; Reed et al., 2012, 2014; Han et al., 2017) as well as the model of Romero-Sarmiento et al., (2013) which suggests the formation of pores from the onset of oil generation. This porosity, probably poorly interconnected and partly filled by entrapped bitumen (not extracted before nitrogen adsorption measurement), does not appear to be accessible by nitrogen

adsorption in KCF mudstones. Hence this porosity was not systematically observed during previous investigations. These new results thus highlight the importance of using complementary methods such as SAXS, a powerful non-destructive global technique, to assess variations of the kerogen structure during the thermal maturation of organic-rich mudstones. This also confirms that the proportion of the unconnected porosity with respect to the open porosity can be very important in this type of reservoirs even in the oil generation stage.

Gas generation (Ro=1.39-2.12%) is characterized by a strong decrease in S, O content and H/C which seems to reach a stable value around ca. 2.2 (Table 2, Figure 1). This chemical transformation is accompanied by a progressive and strong aromatization of kerogen to form a more stable structure shown by the significant decrease in Raman 'disordered' D band areas and intensities and the increase in the 'graphitic' G band resolution (Figures 3, 6). At these maturity stages, OM appears thus as a carbon-rich residue whose structure is increasingly ordered. This concomitant evolution of chemical structure and composition is accompanied by significant changes of the AOM texture in TEM and SEM observations and strong variations of the isolated OM porosity (Table 5). From the condensate/wet gas to the dry gas zone, the amorphous particles exhibit a very granular texture which appears highly heterogeneous down to the nano-scale (Figures 8D-F, 11B, C, F, H). At the higher maturity stage, OM appears to be mainly composed of an agglomeration of grains in SEM (Figure 8E, F). TEM observations reveal the presence of isolated concentric OM grains 50 to 200 nm in diameter dispersed in diffuse heterogeneous amorphous OM particles (Figure 11B-D). These concentric nanostructures were previously described in the Barnett shale (Romero-Sarmiento et al., 2014) and are known to be derived from the secondary cracking of the retained hydrocarbons (Alfè et al., 2009). These structures may thus correspond to pyrobitumen, often described as the main

contributor to the porosity of organic-rich mudstones (Bernard et al., 2012b; Milliken et al., 2013; Hackley and Cardott, 2016; Hackley, 2017). These general variations in OM structure and the formation of these concentric OM nanostructures, visible at the TEM observation scale, may be responsible for the OM-hosted pore development showed by SAXS data and previously observed in total rock KCF mudstones by Cavelan et al., (2019a) during gas generation. This well substantiated the observations of Keel (2015) and Romero-Sarmiento et al. (2014). Keel (2015) suggested that the increase in aromaticity and the ensuing reorganization of kerogen macromolecules with increasing maturity may result in the formation of aromatic 'islands' separated by void spaces formed in response to the expulsion of volatiles. Alternatively, Romero-Sarmiento et al. (2014) demonstrated that the reorientation and the stacking of some structural formed in these concentric residual OM particles during gas generation are responsible for the formation of OM-hosted nanopores in the Barnett Mudstones. The changes in kerogen nanostructure that occur from the peak oil generation to the dry gas zone in SEM and TEM are indeed accompanied by significant variations in the porosity, the specific surface area and the mean pore size of the isolated OM (Table 5). Pores are about 11-13 nm in diameter (Table 5). The continuous increase in the kerogen density, Q, the rising RBS and the relative decrease in the area and intensity of disordered Raman D bands (Table 4, Figures 5, 6), the fluctuations of the porosity, the specific surface area and the mean pore chord indicate that the OM porosity is non-linear during gas generation (Table 5, Figure 12). This may indicate that collapse processes occur in OM in response to gas generation, leading to variations in the size and the volume of OM-hosted pores. Note that none of the structured components derived from plant tissues and pyrite framboids exhibit any variations of structure during maturation (Figures 9A-C, 11) and probably make no contribution to the porosity variations observed at these high maturity stages in the KCF.

In accordance with the observations made on the total rock pore volume (Figure 14), OM porosity exhibits strong variations in porosity during oil and gas generation, marked by phases of destruction and growth. The similarity between previous SEM investigations on total rock KCF mudstones porosity (Cavelan et al., 2019a), the evolution of the total rock pore volume and the isolated OM porosity through thermal maturation clearly demonstrates that the evolution of the chemical structure and the composition of kerogen during maturation seems to be the main factor responsible for the development and the evolution of pores in these organic-rich mudstones. Furthermore, the high porosity of OM (up to ca. 20%) indicates that OM is indeed a significant contributor to the porosity, and thus to the gas storage capacity of mudstone reservoirs. This is in agreement with recent work which showed the strong influence of OM on the porosity and gas adsorption of mudstone reservoirs (Ju et al., 2019, Mastalerz et al., 2013; Song et al., 2019; Yang et al., 2016). However, most of these pores are probably not sufficiently interconnected, explaining why this porosity was not detected by gas adsorption measurements, hence the need to use complementary methods such as SAXS to assess it. In leading to a different original chemical OM structure and variations during thermal maturation (Behar and Vandenbroucke, 1987; Tissot and Welte, 1984) the original kerogen composition between mudstone reservoirs or samples should impact the development of pores, the features of pores or the resulting pore network. This may be especially true for these clay and organic-rich mudstones, where most of the interparticle pores associated with this relatively ductile mineral matrix may be quickly reduced by compaction or filled by entrapped bitumen in the early stages of thermal maturation and where OM thus rapidly becomes the main contributor to the total porosity.

Finally, it's important to note that while the H/C follows the trends observed in the natural environment, the O/C evolve more slowly (Figure 2). We can suggest that the short-duration of our artificial maturation does not allow enough time for the complete reorganization of OM molecules. These reorganization processes that occur in natural environments probably play a predominant role in the organization of the internal structure of the OM carbon network and thus in OM porosity. This may influence the evolution of the ultrafine structure of OM (nanoscopic structure of macerals in TEM and SEM images) and porosity during thermal maturation. For example, Cavelan et al., (2020a) showed that the duration and the temperature used during artificial maturations may influence the thermal degradation kinetics of OM and thus, the evolution of porosity. It is therefore possible that differences exist between the observations made on our experiments and the trend observed in sedimentary basins. Moreover, contrary to SAXS measurements, the total pore volume measured by nitrogen adsorption includes both OM and mineral-hosted porosity. During artificial thermal maturations, the similar variations in the isolated OM porosity and the total pore volume suggest that total pore volume variations are driven by the evolution of the OM porosity in the studied rock, especially during gas generation stages. The duration of our thermal maturations (72 hours) is too short to allow the diagenetic transformations of clay minerals. This is confirmed by a total absence of evolution of the X-ray diffractograms of clay minerals-oriented slides during our experiments. Furthermore, SEM observations of Cavelan et al., (2019a) showed that no changes of the mineral matrix and the associated porosity occur in the same KCF samples during 72 hours-duration artificial maturations (no evidence of dissolution, recrystallization, compaction or reorganization is visible). Therefore, we can assume that the porosity hosted by minerals is relatively constant during our artificial thermal maturations and that OM porosity variations are indeed responsible for most of the

evolution of the total pore volume with increasing maturity. The relative contribution of the OM porosity and thus the total pore volume may however be slightly different in sedimentary basins, where minerals undergo more intense structural and compositional variations with increasing burial.

5. Summary and conclusions

The concomitant evolution of the chemical structure and the porosity of the isolated OM of Kimmeridge clay mudstones during maturation were investigated using a combination of SEM and TEM imaging techniques, Raman spectroscopy and SAXS. The following conclusions were drawn.

(1) Raman spectroscopy, SEM and TEM and SAXS data show that even though the structure of the most mature sample remains relatively disordered, the increase in thermal maturity results in significant densification, reorganization and aromatization of kerogen, predominant in the studied sample. In SEM and TEM, these residual organic components evolved progressively from a relatively homogeneous amorphous structure in immature and early mature samples (Ro ≤ 0.72%) to a granular carbon-rich residue, highly heterogeneous at the nano-scale and containing abundant concentric OM grains (likely pyrobitumens) in overmature samples (Ro of ca. 2.12%). As thermal degradation proceeds, these variations coincide with significant changes in the isolated OM porosity measured by SAXS.

(2) Contrary to the observations previously made on the Kimmeridge clay mudstones and in the total rock studied in this work, the peak of oil generation (Ro of ca. 0.90%) marks the onset of the OM-hosted pore development. This porosity (up to 20%) is probably not sufficiently interconnected or partially field by bitumen and is thus not quantifiable by conventional gas adsorption techniques.

(3) The porosity of the isolated OM shows a complex evolution during gas generation marked by an alternation of collapse processes and pore development.

(4) The similarities existing between the evolution of the total rock pore volume and the isolated OM

porosity through thermal maturation clearly show that the development and evolution of pores and gas

adsorption capacities of these organic-rich mudstones are mainly driven by the evolution of the

chemical structure and the composition of the OM during maturation.

Acknowledgements

References

Alfè, M., Apicella, B., Barbella, R., Rouzaud, J.-N., Tregrossi, A., Ciajolo, A., 2009. Structure–property relationship in nanostructures of young and mature soot in premixed flames. Proceedings of the Combustion Institute 32, 697–704. https://doi.org/10.1016/j.proci.2008.06.193

Ardakani, O.H., Sanei, H., Ghanizadeh, A., Lavoie, D., Chen, Z., Clarkson, C.R., 2018. Do all fractions of organic matter contribute equally in shale porosity? A case study from Upper Ordovician Utica Shale, southern Quebec, Canada. Marine and Petroleum Geology 92, 794–808. https://doi.org/10.1016/j.marpetgeo.2017.12.009

Behar, F., Vandenbroucke, M., 1987. Chemical modelling of kerogens. Organic Geochemistry 11, 15–24. https://doi.org/10.1016/0146-6380(87)90047-7

Bernard, S., Wirth, R., Schreiber, A., Schulz, H.-M., Horsfield, B., 2012. Formation of nanoporous pyrobitumen residues during maturation of the Barnett Shale (Fort Worth Basin). International Journal of Coal Geology 103, 3–11. https://doi.org/10.1016/j.coal.2012.04.010

Bertrand, P., Bordenave, M.L., Brosse, E., Espitalié, J., Houzay, J.P., Pradier, B., Vandenbroucke, M., Walgenwitz, F., 1993. Other methods and tools for source rock appraisal. Applied Petroleum Geochemistry 279–371.

Beyssac, O., Goffé, B., Chopin, C., Rouzaud, J.N., 2002. Raman spectra of carbonaceous material in metasediments: a new geothermometer: RAMAN SPECTROSCOPY OF CARBONACEOUS MATERIAL. Journal of Metamorphic Geology 20, 859–871. https://doi.org/10.1046/j.1525-1314.2002.00408.x

Boulmier, J.L., Oberlin, A., Rouzaud, J.N., Villey, M., 1982. NATURAL ORGANIC MATTERS AND CARBONACEOUS MATERIALS-A PREFERENTIAL FIELD OF APPLICATION FOR TRANSMISSION ELECTRON-MICROSCOPY. Scanning electron microscopy 1523–1538.

Boussafir, M., Gelin, F., Lallier-Vergès, E., Derenne, S., Bertrand, P., Largeau, C., 1995a. Electron microscopy and pyrolysis of kerogens from the Kimmeridge Clay Formation, UK: source organisms, preservation processes, and origin of microcycles. Geochimica et Cosmochimica Acta 59, 3731–3747.

Boussafir, M., Lallier-Vergès, E., 1997. Accumulation of organic matter in the Kimmeridge Clay Formation (KCF): an update fossilisation model for marine petroleum source-rocks. Marine and Petroleum Geology 14, 75–83.

Boussafir, M., Lallier-Vergès, E., Bertrand, P., Badaut-Trauth, D., 1995b. SEM and TEM studies on isolated organic matter and rock microfacies from a short-term organic cycle of the Kimmeridge Clay Formation (Yorkshire, GB). in: Organic Matter Accumulation. Berlin, Heidelberg, pp. 15–30.

Boussafir, M., Lallier-Vergès, E., Bertrand, P., Badaut-Trauth, D., 1994. The ultrafine structure of organic-matter from Kimmeridgian source-rocks of Yorkshire (UK). Bulletin de la Societe Geologique de France 4, 353–361.

Bustin, R.M., Bustin, A., Ross, D.J.K., Chalmers, G.R.L., Murthy, V., Laxmi, C., Cui, X., 2009. Shale gas opportunities and challenges. Presented at the American Association of Petroleum Geologists Annual Convention, San Antonio, TX.

Cavelan, A., Boussafir, M., Le Milbeau, C., Delpeux, S., Laggoun-Défarge, F., 2020a. Influence of experimental temperature and duration of laboratory confined thermal maturation experiments on the evolution of the porosity of organic-rich source rocks. Marine and Petroleum Geology 104667.

Cavelan, A., Boussafir, M., Le Milbeau, C., Laggoun-Défarge, F., 2020b. Impact of Oil-Prone Sedimentary Organic Matter Quality and Hydrocarbon Generation on Source Rock Porosity: Artificial Thermal Maturation Approach. ACS Omega. https://doi.org/10.1021/acsomega.0c01432

Cavelan, A., Boussafir, M., Le Milbeau, C., Rozenbaum, O., Laggoun-Défarge, F., 2019a. Effect of organic matter composition on source rock porosity during confined anhydrous thermal maturation: Example of Kimmeridge-clay mudstones. International Journal of Coal Geology 212. https://doi.org/10.1016/j.coal.2019.103236

Cavelan, A., Boussafir, M., Rozenbaum, O., Laggoun-Défarge, F., 2019b. Organic petrography and pore structure characterization of low-mature and gas-mature marine organic-rich mudstones: Insights into porosity controls in gas shale systems. Marine and Petroleum Geology 103, 331–350.

Chalmers, G.R., Bustin, R.M., Power, I.M., 2012a. Characterization of gas shale pore systems by porosimetry, pycnometry, surface area, and field emission scanning electron microscopy/transmission electron microscopy image analyses: Examples from the Barnett, Woodford, Haynesville, Marcellus, and Doig units. AAPG Bulletin 96, 1099–1119. https://doi.org/10.1306/10171111052

Chalmers, G.R., Bustin, R.M., Power, I.M., 2012b. Characterization of gas shale pore systems by porosimetry, pycnometry, surface area, and field emission scanning electron microscopy/transmission electron microscopy image analyses: Examples from the Barnett,

Woodford, Haynesville, Marcellus, and Doig units. AAPG Bulletin 96, 1099–1119. https://doi.org/10.1306/10171111052

Chalmers, G.R.L., Bustin, R.M., 2008. Lower Cretaceous gas shales in northeastern British Columbia, Part I: geological controls on methane sorption capacity. Bulletin of Canadian Petroleum Geology 56, 1–21. https://doi.org/10.2113/gscpgbull.56.1.1

Chen, J., Xiao, X., 2014. Evolution of nanoporosity in organic-rich shales during thermal maturation. Fuel 129, 173–181. https://doi.org/10.1016/j.fuel.2014.03.058

Chen, Z., Wang, T., Liu, Q., Zhang, S., Zhang, L., 2015. Quantitative evaluation of potential organic-matter porosity and hydrocarbon generation and expulsion from mudstone in continental lake basins: A case study of Dongying sag, eastern China. Marine and Petroleum Geology 66, 906–924.

Cheshire, S., Craddock, P.R., Xu, G., Sauerer, B., Pomerantz, A.E., McCormick, D., Abdallah, W., 2017. Assessing thermal maturity beyond the reaches of vitrinite reflectance and Rock-Eval pyrolysis: A case study from the Silurian Qusaiba formation. International Journal of Coal Geology 180, 29–45. https://doi.org/10.1016/j.coal.2017.07.006

Clarkson, C.R., Solano, N., Bustin, R.M., Bustin, A.M.M., Chalmers, G.R.L., He, L., Melnichenko, Y.B., Radliński, A.P., Blach, T.P., 2013. Pore structure characterization of North American shale gas reservoirs using USANS/SANS, gas adsorption, and mercury intrusion. Fuel 103, 606–616. https://doi.org/10.1016/j.fuel.2012.06.119

Cohaut, N., Blanche, C., Dumas, D., Guet, J.M., Rouzaud, J.N., 2000. A small angle X-ray scattering study on the porosity of anthracites. Carbon 38, 1391–1400.

Cornford, C., 1984. Source rocks and hydrocarbons of the North Sea. In: Glennie, K.W. (Ed.), Introduction to the Petroleum Geology of the North Sea. Blackwell Scientific Publications, Oxford 171–209.

Curtis, M.E., Cardott, B.J., Sondergeld, C.H., Rai, C.S., 2012. Development of organic porosity in the Woodford Shale with increasing thermal maturity. International Journal of Coal Geology 103, 26–31. https://doi.org/10.1016/j.coal.2012.08.004

Ferrari, A.C., Robertson, J., 2000. Interpretation of Raman spectra of disordered and amorphous carbon. Phys. Rev. B 61, 14095–14107. https://doi.org/10.1103/PhysRevB.61.14095

Fishman, N.S., Hackley, P.C., Lowers, H.A., Hill, R.J., Egenhoff, S.O., Eberl, D.D., Blum, A.E., 2012. The nature of porosity in organic-rich mudstones of the Upper Jurassic Kimmeridge Clay Formation, North Sea, offshore United Kingdom. International Journal of Coal Geology 103, 32–50. https://doi.org/10.1016/j.coal.2012.07.012

Furmann, A., Mastalerz, M., Bish, D., Schimmelmann, A., Pedersen, P.K., 2016. Porosity and pore size distribution in mudrocks from the Belle Fourche and Second White Specks Formations in Alberta, Canada. Bulletin 100, 1265–1288. https://doi.org/10.1306/02191615118

Gallois, R., 2004. The Kimmeridge Clay: the most intensively studied formation in Britain. Journal Open University Geological Society 25, 33–38.

Gelin, F., Boussafir, M., Derenne, S., Largeau, C., Bertrand, P., 1995. Study of qualitative and quantitative variations in kerogen chemical structure along a microcycle: correlations with ultrastructural features., in: Organic Matter Accumulation. pp. 31–47.

Ghanizadeh, A., Clarkson, C.R., Clarke, K.M., Yang, Z., Rashidi, B., Vahedian, A., Song, C., DeBuhr, C., Haghshenas, B., Ardakani, O.H., 2020. Effects of Entrained Hydrocarbon and Organic-Matter Components on Reservoir Quality of Organic-Rich Shales: Implications for "Sweet Spot" Identification and Enhanced-Oil-Recovery Applications in the Duvernay Formation (Canada). SPE Journal.

Guo, H., He, R., Jia, W., Peng, P., Lei, Y., Luo, X., Wang, X., Zhang, L., Jiang, C., 2018. Pore characteristics of lacustrine shale within the oil window in the Upper Triassic Yanchang Formation, southeastern Ordos Basin, China. Marine and Petroleum Geology 91, 279–296. https://doi.org/10.1016/j.marpetgeo.2018.01.013

Hackley, P.C., 2017. Application of Organic Petrology in High Maturity Shale Gas Systems, in: Geology: Current and Future Developments: The Role of Organic Petrology in the Exploration of Conventional and Unconventional Hydrocarbon Systems. sabel Suárez-Ruiz and João Graciano Mendonça Filho, Sharjah, UAE, pp. 205–235.

Hackley, P.C., Cardott, B.J., 2016. Application of organic petrography in North American shale petroleum systems: A review. International Journal of Coal Geology 163, 8–51. https://doi.org/10.1016/j.coal.2016.06.010

Hackley, P.C., Zhang, L., Zhang, T., 2017. Organic petrology of peak oil maturity Triassic Yanchang Formation lacustrine mudrocks, Ordos Basin, China. Interpretation 5, SF211–SF223. https://doi.org/10.1190/INT-2016-0111.1

Han, H., Pang, P., Li, Z., Shi, P., Guo, C., Liu, Y., Chen, S., Lu, J., Gao, Y., 2019. Controls of organic and inorganic compositions on pore structure of lacustrine shales of Chang 7 member from Triassic Yanchang Formation in the Ordos Basin, China. Marine and Petroleum Geology 100, 270–284. https://doi.org/10.1016/j.marpetgeo.2018.10.038

Han, Y., Horsfield, B., Wirth, R., Mahlstedt, N., Bernard, S., 2017. Oil retention and porosity evolution in organic-rich shales. Bulletin 101, 807–827. https://doi.org/10.1306/09221616069

Herbin, J.P., Fernandez-Martinez, J.L., Geyssant, J.R., Albani, A.El., Deconinck, J.F., Proust, J.N., Colbeaux, J.P., Vidier, J.P., 1995. Sequence stratigraphy of source rocks applied to the study of the Kimmeridgian/Tithonian in the north-west European shelf (Dorset/UK, Yorkshire/UK and Boulonnais/France). Marine and Petroleum Geology 12, 177–194. https://doi.org/10.1016/0264-8172(95)92838-N

Ju, Y., He, J., Chang, E., Zheng, L., 2019. Quantification of CH4 adsorption capacity in kerogen-rich reservoir shales: An experimental investigation and molecular dynamic simulation. Energy 170, 411–422. https://doi.org/10.1016/j.energy.2018.12.087

Katz, B.J., Arango, I., 2018. Organic porosity: A geochemist's view of the current state of understanding. Organic Geochemistry 123, 1–16. https://doi.org/10.1016/j.orggeochem.2018.05.015

Keel, M.B., 2015. Organic Porosity Distribution as Function of Aromaticity in Organic-Rich Mudrocks. University of Kansas.

King, Jr., H.E., Eberle, A.P.R., Walters, C.C., Kliewer, C.E., Ertas, D., Huynh, C., 2015. Pore Architecture and Connectivity in Gas Shale. Energy Fuels 29, 1375–1390.

Klaver, J., Desbois, G., Littke, R., Urai, J.L., 2015. BIB-SEM characterization of pore space morphology and distribution in postmature to overmature samples from the Haynesville and Bossier Shales. Marine and petroleum Geology 59, 451–466.

Ko, L.T., Loucks, R.G., Milliken, K.L., Liang, Q., Zhang, T., Sun, X., Hackley, P.C., Ruppel, S.C., Peng, S., 2017. Controls on pore types and pore-size distribution in the Upper Triassic Yanchang Formation, Ordos Basin, China: Implications for pore-evolution models of lacustrine mudrocks. Interpretation 5, SF127–SF148. https://doi.org/10.1190/INT-2016-0115.1

Ko, L.T., Ruppel, S.C., Loucks, R.G., Hackley, P.C., Zhang, T., Shao, D., 2018. Pore-types and pore-network evolution in Upper Devonian-Lower Mississippian Woodford and Mississippian Barnett mudstones: Insights from laboratory thermal maturation and organic petrology. International Journal of Coal Geology 190, 3–28. https://doi.org/10.1016/j.coal.2017.10.001

Kuila, U., McCarty, D.K., Derkowski, A., Fischer, T.B., Prasad, M., 2014. Total porosity measurement in gas shales by the water immersion porosimetry (WIP) method. Fuel 117, 1115–1129. https://doi.org/10.1016/j.fuel.2013.09.073

Kuila, U., Prasad, M., Derkowski, A., McCarty, D.K., 2012. Compositional controls on mudrock pore-size distribution: An example from Niobrara Formation, in: SPE Annual Technical Conference and Exhibition. Society of Petroleum Engineers.

Lallier-Vergès, E., Bertrand, B., Tribovillard, N., 1995. Short-term organic cyclicities from the Kimmeridge Clay Formation of Yorkshire (G.B.): combined accumulation and degradation of organic carbon under the control of primary production variations | SpringerLink, in: In Organic Matter Accumulation. Berlin, Heidelberg, pp. 3–13.

Leu, L., Georgiadis, A., Blunt, M.J., Busch, A., Bertier, P., Schweinar, K., Liebi, M., Menzel, A., Ott, H., 2016. Multiscale Description of Shale Pore Systems by Scanning SAXS and WAXS Microscopy. Energy Fuels 30, 10282–10297. https://doi.org/10.1021/acs.energyfuels.6b02256

Li, X., Hayashi, J., Li, C., 2006. FT-Raman spectroscopic study of the evolution of char structure during the pyrolysis of a Victorian brown coal. Fuel 85, 1700–1707. https://doi.org/10.1016/j.fuel.2006.03.008

Lin-Vien, D., Colthup, N.B., Fateley, W.G., Grasselli, J.G., 1991. The handbook of infrared and Raman characteristic frequencies of organic molecules. Elsevier.

Liu, D., Xiao, X., Tian, H., Min, Y., Zhou, Q., Cheng, P., Shen, J., 2013. Sample maturation calculated using Raman spectroscopic parameters for solid organics: Methodology and geological applications. Chin. Sci. Bull. 58, 1285–1298. https://doi.org/10.1007/s11434-012-5535-y

Liu, K., Ostadhassan, M., Zhou, J., Gentzis, T., Rezaee, R., 2017. Nanoscale pore structure characterization of the Bakken shale in the USA. Fuel 209, 567–578. https://doi.org/10.1016/j.fuel.2017.08.034

Liu, Y., Xiong, Y., Li, Y., Peng, P.A., 2018. Effect of thermal maturation on chemical structure and nanomechanical properties of solid bitumen. Marine and Petroleum Geology 92, 780–793.

Löhr, S.C., Baruch, E.T., Hall, P.A., Kennedy, M.J., 2015. Is organic pore development in gas shales influenced by the primary porosity and structure of thermally immature organic matter? Organic Geochemistry 87, 119–132. https://doi.org/10.1016/j.orggeochem.2015.07.010

Loucks, R.G., Reed, R.M., Ruppel, S.C., Hammes, U., 2012. Spectrum of pore types and networks in mudrocks and a descriptive classification for matrix-related mudrock pores. Bulletin 96, 1071–1098. https://doi.org/10.1306/08171111061

Loucks, R.G., Reed, R.M., Ruppel, S.C., Jarvie, D.M., 2009. Morphology, Genesis, and Distribution of Nanometer-Scale Pores in Siliceous Mudstones of the Mississippian Barnett Shale. Journal of Sedimentary Research 79, 848–861. https://doi.org/10.2110/jsr.2009.092

Ma, Y., Zhong, N., Li, D., Pan, Z., Cheng, L., Liu, K., 2015. Organic matter/clay mineral intergranular pores in the Lower Cambrian Lujiaping Shale in the north-eastern part of the upper Yangtze area, China: A possible microscopic mechanism for gas preservation. International Journal of Coal Geology 137, 38–54. https://doi.org/10.1016/j.coal.2014.11.001

Mastalerz, M., Schimmelmann, A., Drobniak, A., Chen, Y., 2013. Porosity of Devonian and Mississippian New Albany Shale across a maturation gradient: Insights from organic petrology, gas adsorption, and mercury intrusion. AAPG Bulletin 97, 1621–1643. https://doi.org/10.1306/04011312194

Mastalerz, M., Schimmelmann, A., Lis, G.P., Drobniak, A., Stankiewicz, A., 2012. Influence of maceral composition on geochemical characteristics of immature shale kerogen: Insight from density fraction analysis. International Journal of Coal Geology 103, 60–69. https://doi.org/10.1016/j.coal.2012.07.011

Mathia, E.J., Bowen, L., Thomas, K.M., Aplin, A.C., 2016. Evolution of porosity and pore types in organic-rich, calcareous, Lower Toarcian Posidonia Shale. Marine and Petroleum Geology 75, 117–139. https://doi.org/10.1016/j.marpetgeo.2016.04.009

Mernagh, T.P., Cooney, R.P., Johnson, R.A., 1984. Raman spectra of Graphon carbon black. Carbon 22, 39–42. https://doi.org/10.1016/0008-6223(84)90130-1

Milliken, K.L., Rudnicki, M., Awwiller, D.N., Zhang, T., 2013. Organic matter-hosted pore system, Marcellus Formation (Devonian), Pennsylvania. Bulletin 97, 177–200. https://doi.org/10.1306/07231212048

Oberlin, A., 1989. High-resolution TEM studies of carbonization and graphitization. Chemistry and physics of carbon 22.

Pan, L., Xiao, X., Tian, H., Zhou, Q., Chen, J., Li, T., Wei, Q., 2015. A preliminary study on the characterization and controlling factors of porosity and pore structure of the Permian shales in Lower Yangtze region, Eastern China. International Journal of Coal Geology 146, 68–78. https://doi.org/10.1016/j.coal.2015.05.005

Peters, K.E., Walters, C.C., Moldowan, J.M., Peters, K.E., 2007. Biomarkers and isotopes in the environment and human history, 2. ed., reprinted with corrections, digitally printed version 2007. ed, The biomarker guide. Cambridge Univ. Press, Cambridge, UK.

Quirico, E., Rouzaud, J.-N., Bonal, L., Montagnac, G., 2005. Maturation grade of coals as revealed by Raman spectroscopy: Progress and problems. Spectrochimica Acta Part A: Molecular and Biomolecular Spectroscopy 61, 2368–2377. https://doi.org/10.1016/j.saa.2005.02.015

Rawson, P.F., Riley, L.A., 1982. Latest Jurassic - Early Cretaceous Events and the "Late Cimmerian Unconformity" in North Sea Area. AAPG Bulletin, AAPG Bulletin 66, 2628–2648.

Rebelo, S.L.H., Guedes, A., Szefczyk, M.E., Pereira, A.M., Araújo, J.P., Freire, C., 2016. Progress in the Raman spectra analysis of covalently functionalized multiwalled carbon nanotubes: unraveling disorder in graphitic materials. Phys. Chem. Chem. Phys. 18, 12784–12796. https://doi.org/10.1039/C5CP06519D

Reed, R.M., 2017. Organic-matter pores: new findings from lower-thermal maturity mudrocks. GCAGS Journal 6, 99–110.

Reed, R.M., Loucks, R.G., Milliken, K.L., 2012. Heterogeneity of shape and microscale spatial distribution in organic-matter-hosted pores of gas shales. Presented at the Proceedings AAPG Annual Convention and Exhibition.

Reed, R.M., Loucks, R.G., Ruppel, S.C., 2014. Comment on "Formation of nanoporous pyrobitumen residues during maturation of the Barnett Shale (Fort Worth Basin)" by Bernard et al. (2012). International Journal of Coal Geology 127, 111–113. https://doi.org/10.1016/j.coal.2013.11.012

Robert, P., 1971. Etude pétrographique des matières organiques insolubles par la mesure de leur pouvoir reflecteur. Contribution à l'exploration petrolière et à la connaissare des basins sédimentaires. Revue Institut Français Pétrole 26, 105–136.

Rodriguez, R., Crandall, D., Song, X., Verba, C., Soeder, D., 2014. Imaging techniques for analyzing shale pores and minerals. (No. NETL-TRS-6). National Energy Technology Laboratory, Morgantown, WV, USA.

Romero-Sarmiento, M.-F., Ducros, M., Carpentier, B., Lorent, F., Cacas, M.-C., Pegaz-Fiornet, S., Wolf, S., Rohais, S., Moretti, I., 2013. Quantitative evaluation of TOC, organic porosity and gas retention distribution in a gas shale play using petroleum system modeling: Application to the Mississippian Barnett Shale. Marine and Petroleum Geology 45, 315–330. https://doi.org/10.1016/j.marpetgeo.2013.04.003

Romero-Sarmiento, M.-F., Rouzaud, J.-N., Bernard, S., Deldicque, D., Thomas, M., Littke, R., 2014. Evolution of Barnett Shale organic carbon structure and nanostructure with increasing maturation. Organic Geochemistry 71, 7–16. https://doi.org/10.1016/j.orggeochem.2014.03.008

Ross, D.J.K., Bustin, M.R., 2009. The importance of shale composition and pore structure upon gas storage potential of shale gas reservoirs. Marine and Petroleum Geology 26, 916–927. https://doi.org/10.1016/j.marpetgeo.2008.06.004

Rouquerol, J., Avnir, D., Fairbridge, C.W., Everett, D.H., Haynes, J.M., Pernicone, N., Ramsay, J.D.F., Sing, K.S.W., Unger, K.K., 1994. Recommendations for the characterization of porous solids (Technical Report). Pure and Applied Chemistry 66, 1739–1758.

Rouzaud, J.N., Oberlin, A., 1989. Structure, microtexture, and optical properties of anthracene and saccharose-based carbons. Carbon 27, 517–529. https://doi.org/10.1016/0008-6223(89)90002-X

Sadezky, A., Muckenhuber, H., Grothe, H., Niessner, R., Pöschl, U., 2005. Raman microspectroscopy of soot and related carbonaceous materials: Spectral analysis and structural information. Carbon 43, 1731–1742. https://doi.org/10.1016/j.carbon.2005.02.018

Sauerer, B., Craddock, P.R., AlJohani, M.D., Alsamadony, K.L., Abdallah, W., 2017. Fast and accurate shale maturity determination by Raman spectroscopy measurement with minimal sample preparation. International Journal of Coal Geology 173, 150–157. https://doi.org/10.1016/j.coal.2017.02.008

Schito, A., Romano, C., Corrado, S., Grigo, D., Poe, B., 2017. Diagenetic thermal evolution of organic matter by Raman spectroscopy. Organic Geochemistry 106, 57–67. https://doi.org/10.1016/j.orggeochem.2016.12.006

Song, L., Martin, K., Carr, T.R., Ghahfarokhi, P.K., 2019. Porosity and storage capacity of Middle Devonian shale: A function of thermal maturity, total organic carbon, and clay content. Fuel 241, 1036–1044. https://doi.org/10.1016/j.fuel.2018.12.106

Strąpoć, D., Mastalerz, M., Schimmelmann, A., Drobniak, A., Hasenmueller, N.R., 2010. Geochemical constraints on the origin and volume of gas in the New Albany Shale (Devonian–Mississippian), eastern Illinois Basin. Bulletin 94, 1713–1740. https://doi.org/10.1306/06301009197

Tian, H., Pan, L., Xiao, X., Wilkins, R.W.T., Meng, Z., Huang, B., 2013. A preliminary study on the pore characterization of Lower Silurian black shales in the Chuandong Thrust Fold Belt, southwestern China using low pressure N2 adsorption and FE-SEM methods. Marine and Petroleum Geology 48, 8–19. https://doi.org/10.1016/j.marpetgeo.2013.07.008

Tian, H., Pan, L., Zhang, T., Xiao, X., Meng, Z., Huang, B., 2015. Pore characterization of organic-rich Lower Cambrian shales in Qiannan Depression of Guizhou Province, Southwestern China. Marine and Petroleum Geology 62, 28–43. https://doi.org/10.1016/j.marpetgeo.2015.01.004

Tissot, B.P., Pelet, R., Ungerer, P., 1987. Thermal History of Sedimentary Basins, Maturation Indices, and Kinetics of Oil and Gas Generation. Bulletin 71. https://doi.org/10.1306/703C80E7-1707-11D7-8645000102C1865D

Tissot, Welte, D.H., 1984. Petroleum formation and occurence, 2. rev. and enl. ed. ed. Springer, Berlin, Heidelberg [usw.].

Tribovillard, N., Bialkowski, A., Tyson, R.V., Lallier-Vergès, E., Deconinck, J.-F., 2001. Organic facies variation in the late Kimmeridgian of the Boulonnais area (northernmost France). Marine and Petroleum Geology 18, 371–389. https://doi.org/10.1016/S0264-8172(01)00006-X

Tuinstra, F., Koenig, J.L., 1970. Raman Spectrum of Graphite. The Journal of Chemical Physics 53, 1126–1130. https://doi.org/10.1063/1.1674108

Wang, F., Guan, J., Feng, W., Bao, L., 2013. Evolution of overmature marine shale porosity and implication to the free gas volume. Petroleum Exploration and Development 40, 819–824. https://doi.org/10.1016/S1876-3804(13)60111-1

Yang, F., Ning, Z., Wang, Q., Zhang, R., Krooss, B.M., 2016. Pore structure characteristics of lower Silurian shales in the southern Sichuan Basin, China: Insights to pore development and gas storage mechanism. International Journal of Coal Geology 156, 12–24. https://doi.org/10.1016/j.coal.2015.12.015

Author statement

Amelie Cavelan : Investigation - Original draft preparation- Redaction - Writing - Review & Editing.

Mohammed Boussafir : Conceptualization - Redaction -Supervision- Review & Editing - Funding

acquisition. **Nathalie Mathieu** : Methodology – Investigation -Validation – Reviewing. **Fatima**

Laggoun-Défarge : Supervision – Project administration – Conceptualization- Supervision.

Declaration of interests

☒ The authors declare that they have no known competing financial interests or personal relationships

that could have appeared to influence the work reported in this paper.

☐The authors declare the following financial interests/personal relationships which may be considered as potential competing interests:

Highlights

- Impact of artificial maturation on the evolution of the OM ultrafine structure.

- SAXS allows the assessment of connected and non-connected pore volume.

- The peak of oil generation marks the onset of pores development in OM.

- OM and total rock pore volumes show a similar evolution in the gas window.
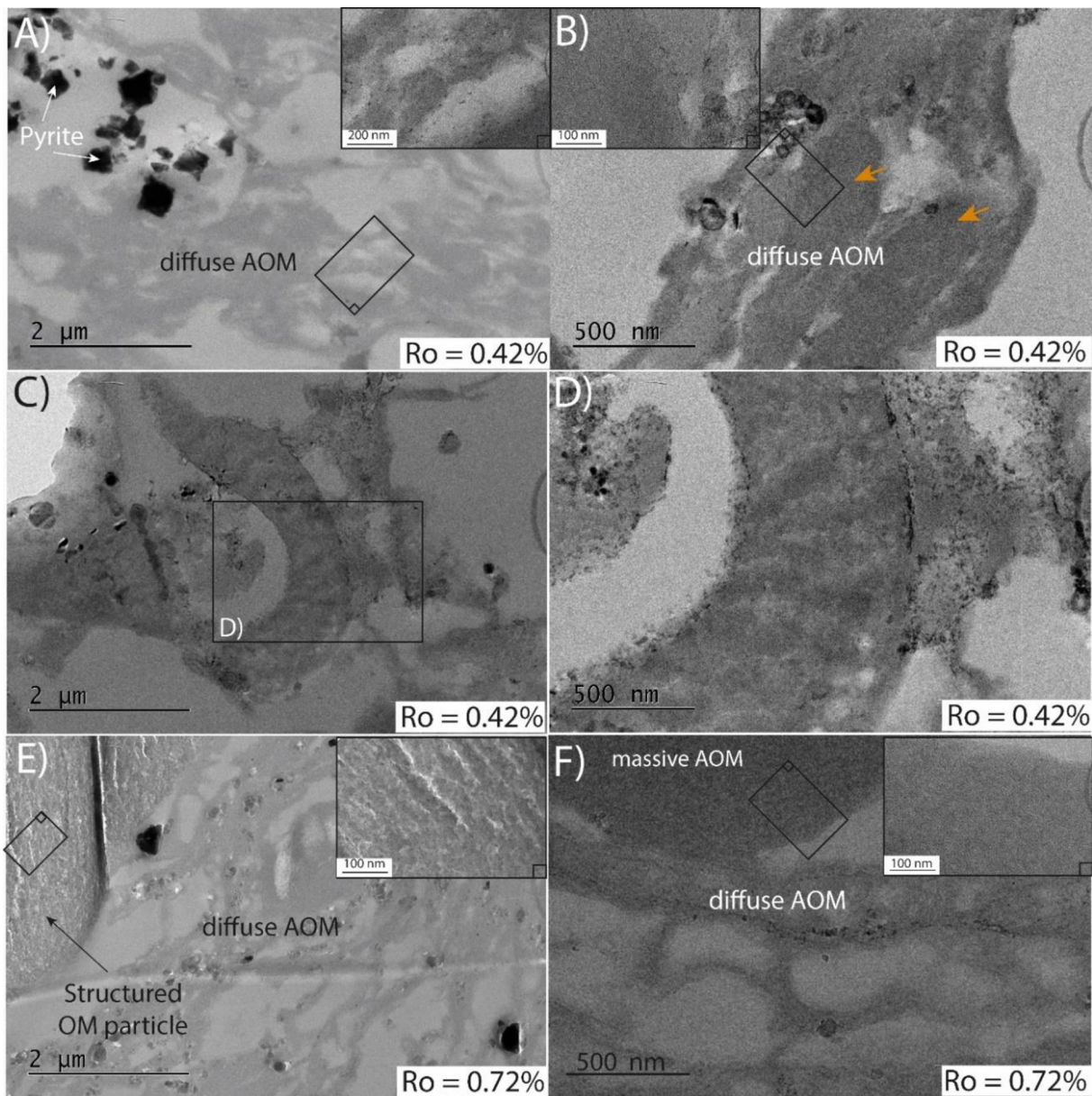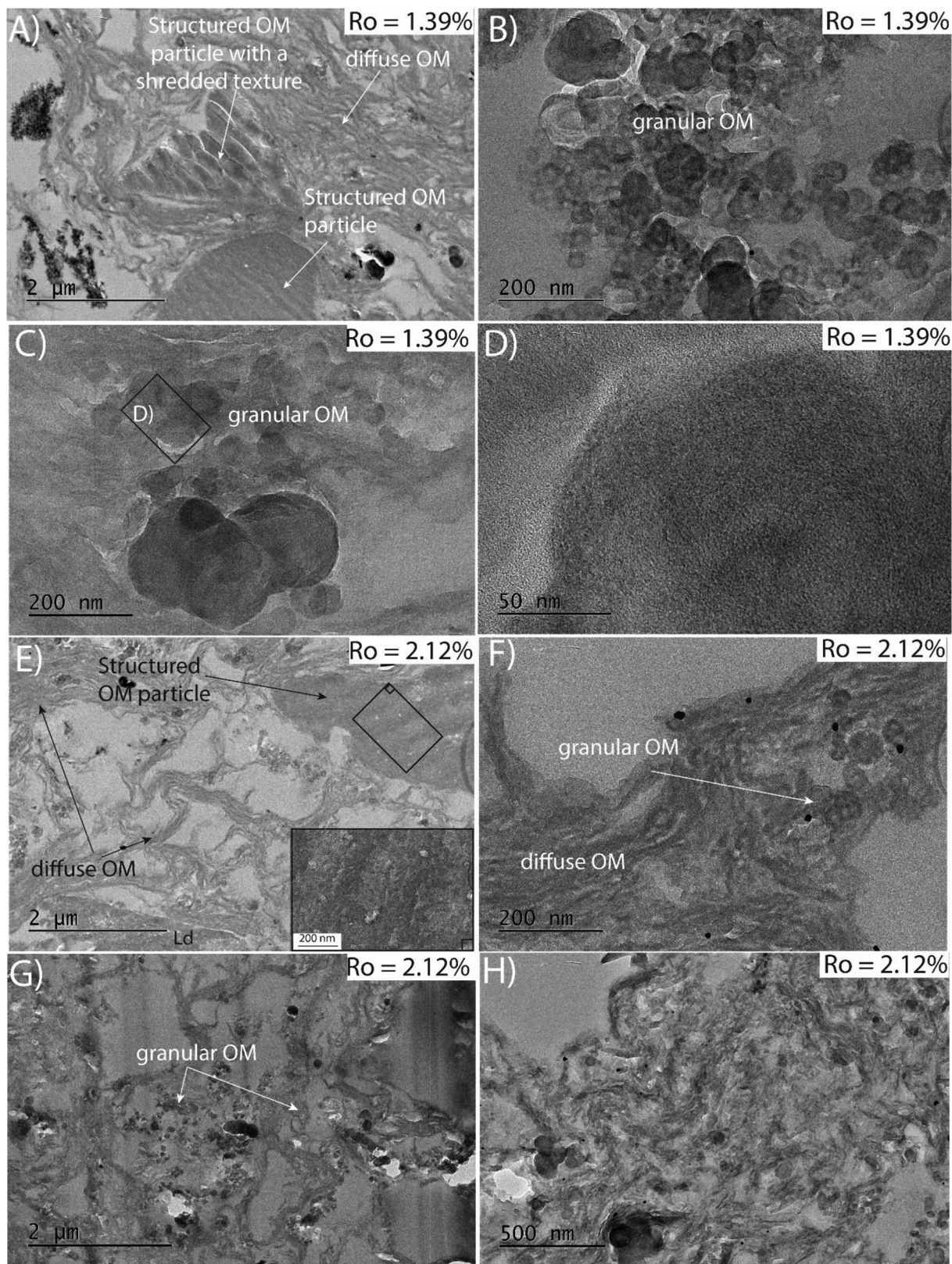
- Mudstones porosity is mainly driven by the OM chemical structure during maturation.
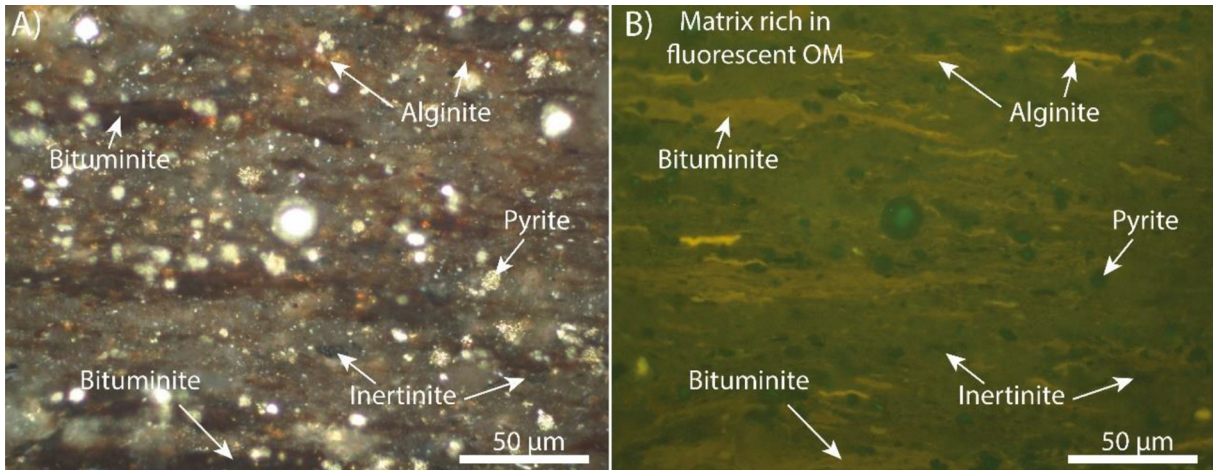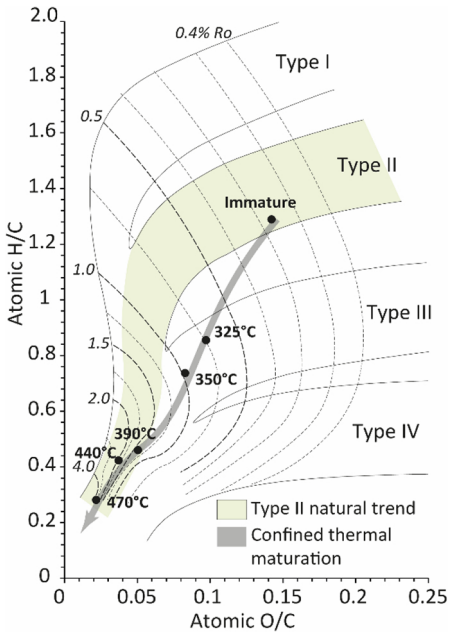
Figure 1

Figure 2
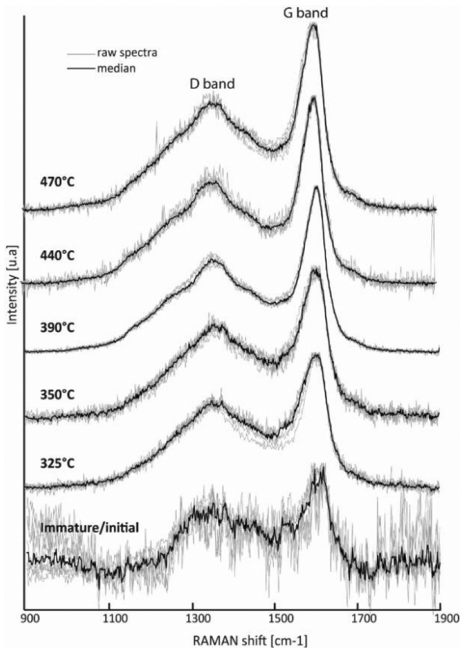
Figure 3
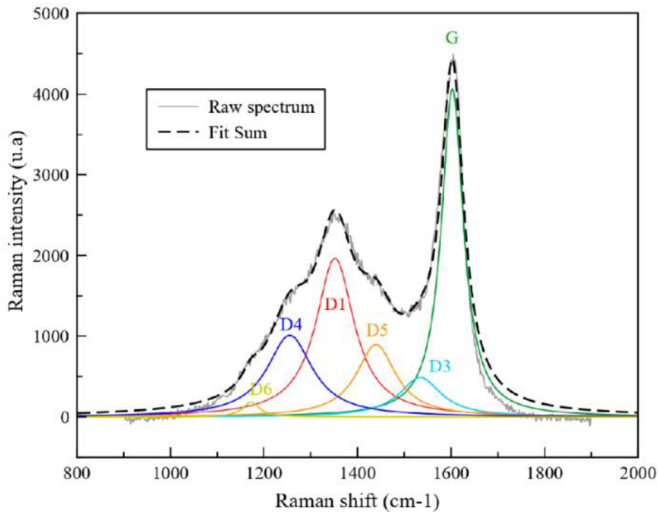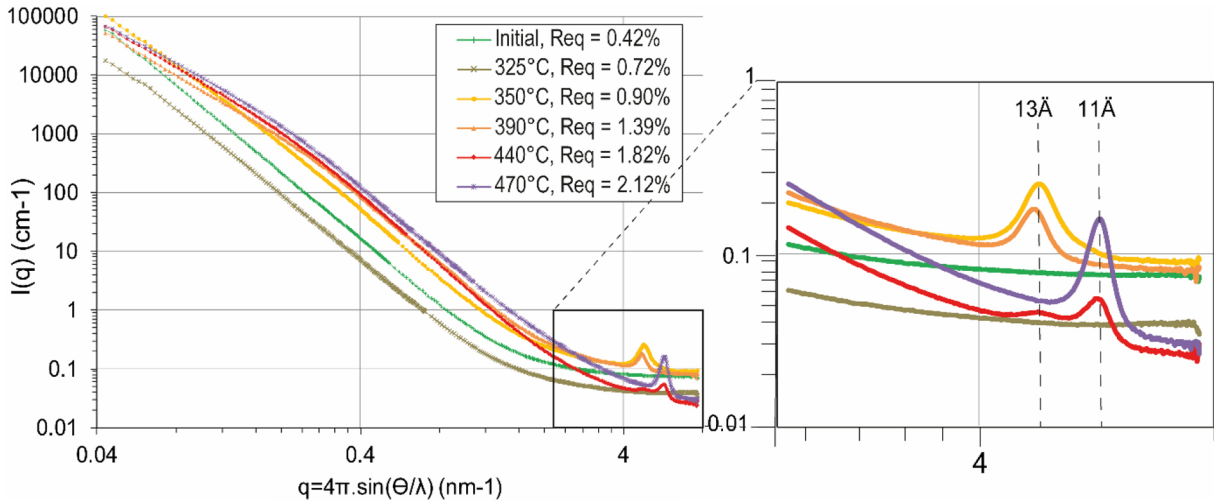
Figure 4
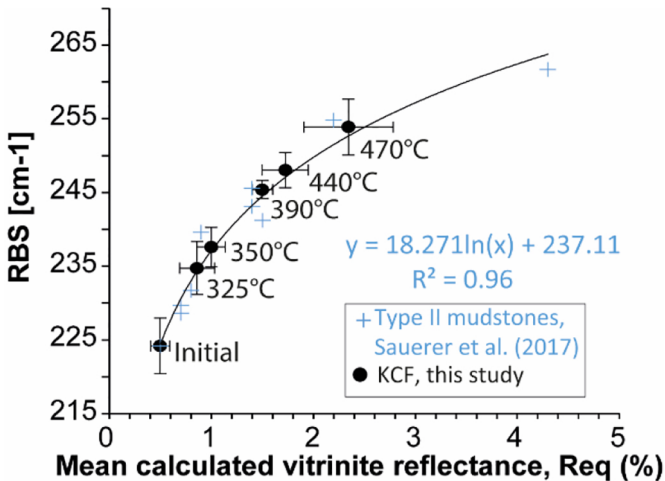
Figure 5
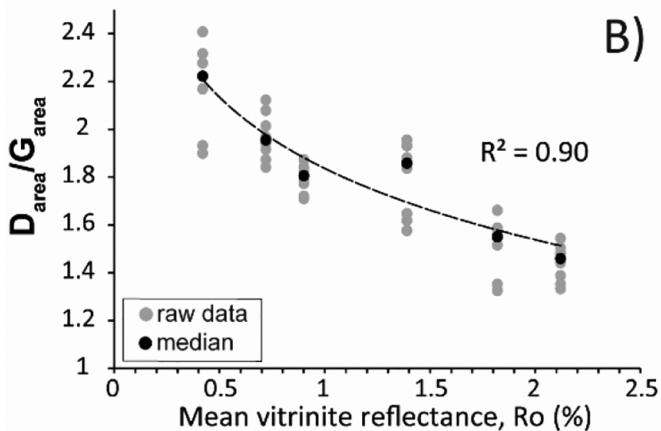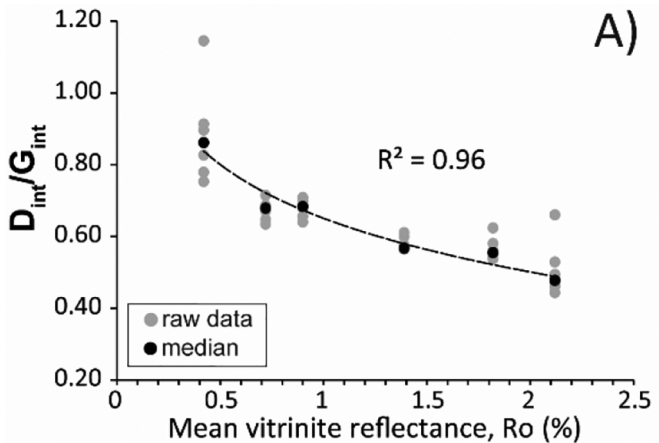
Figure 6
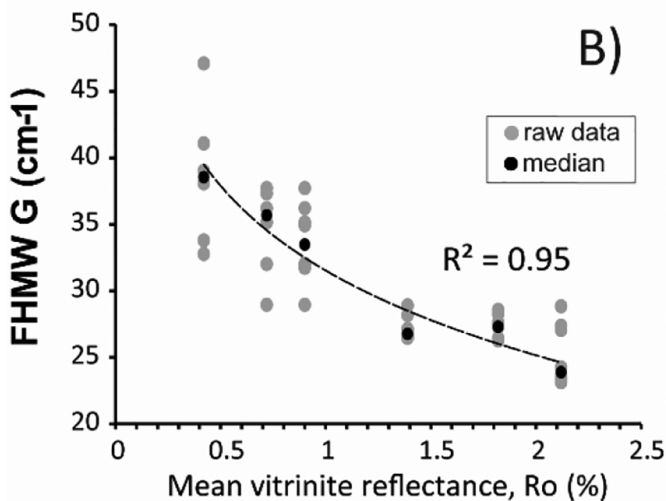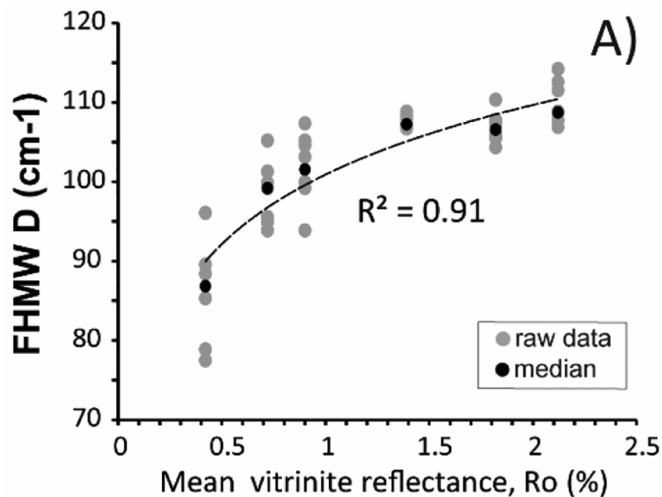
Figure 7
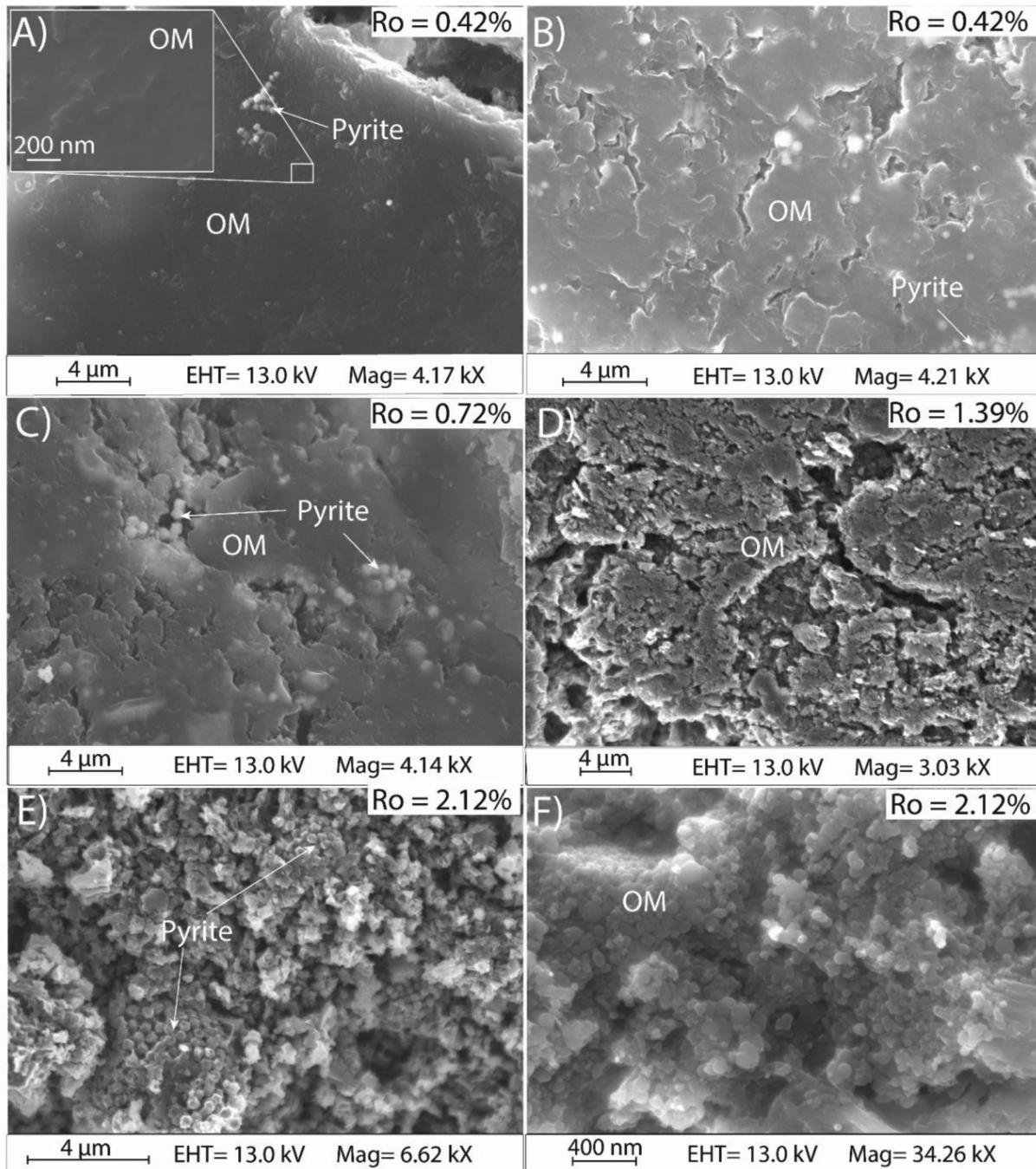
Figure 8
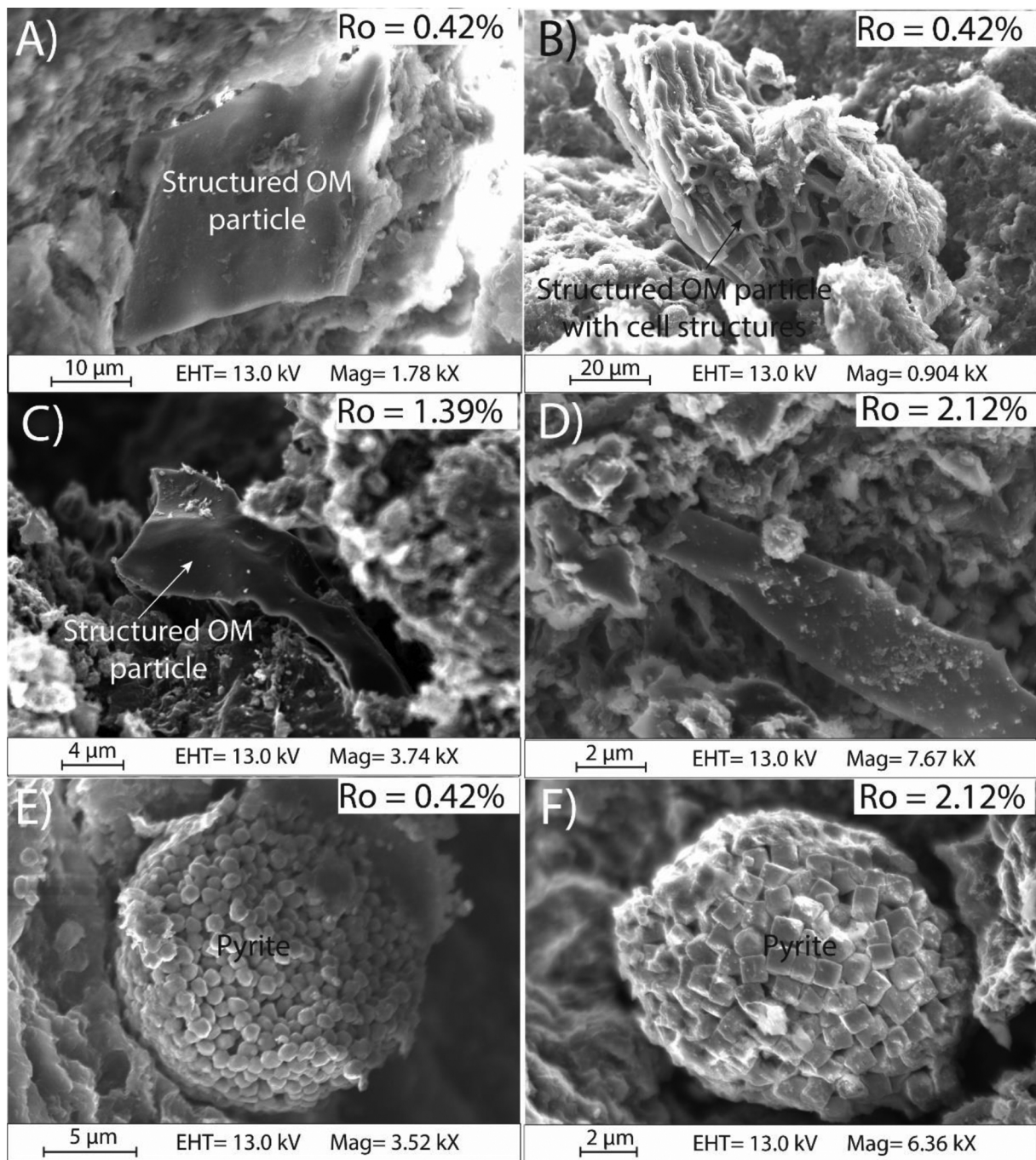
Figure 9

Figure 10

Figure 11

Figure 12

Figure 13

Figure 14